



Eidgenössische Technische Hochschule Zürich  
Swiss Federal Institute of Technology Zurich

# HR 8799 imaged in the long I band

Master thesis

Dominique Gisin

March - September 2021

Advisors: Christian Tschudi, Prof. Hans Martin Schmid  
Institute for Particle Physics and Astrophysics, ETH Zürich



---

## Abstract

In this thesis we analyzed directly imaged data of the HR 8799 exoplanet system in the long I band, collected by the ZIMPOL instrument. Our obtained contrast limits of  $C = 0.12 \cdot 10^{-6}$  (HR 8799 b) till  $C = 7.9 \cdot 10^{-6}$  (HR 8799 e) did not allow a confirmation of any of the four known exoplanets with a  $S/N > 3$  at the interpolated exoplanet positions at time of observation.

Our methods showed that the contrast limit is lowered by a factor of 2-5 when combining multiple data sets, observed at different times. The improvement is more pronounced close to the host star. The factor is in the range of the expected theoretical factor for the longer total exposure times.

When applying a simple ADI mean subtraction of the data, the contrast limit is again lowered by a factor of 2 compared to the combined stacked and averaged data sets. A frame selection of the data sets is not lowering the contrast limit significantly.

Compared to the known measured contrast limits of the four exoplanets, we see, that our contrast limit for HR 8799 d and HR 8799 e is well above the expected contrast. For HR 8799 b and HR 8799 c our contrast limit is within the range of the contrast expected by models in the long I band. With more integrations (better subtraction of the static PSF structure) and longer individual frame exposures (less read out noise) a detection of the exoplanets HR 8799 c and HR 8799 b should be feasible with the ZIMPOL instrument with the expected exoplanet emission in the long I band.



---

## Acknowledgements

---

A big thanks to Professor Hans Martin Schmid and my supervisor Christian Tschudi for all the time and energy they invested into our weekly meetings. It was a very motivating and effective setup. A special thanks to Christian Tschudi for all his tipps and tricks and his patience with my rather mediocre programming skills.

I also want to thank the SPHERE/ZIMPOL collaboration for providing me with the observation data used in this analysis.



---

# Contents

---

<b>Acknowledgements</b>	<b>iii</b>
<b>Contents</b>	<b>v</b>
<b>List of Figures</b>	<b>vii</b>
<b>List of Tables</b>	<b>ix</b>
<b>1 Introduction</b>	<b>1</b>
1.1 Stellar properties of HR 8799 . . . . .	2
<b>2 Measurement &amp; Methods</b>	<b>5</b>
2.1 SPHERE / ZIMPOL . . . . .	5
2.1.1 Angular differential imaging (ADI) . . . . .	6
2.1.2 Observed data properties . . . . .	7
2.2 Astrometry . . . . .	8
2.3 Aperture photometry . . . . .	11
2.3.1 Signal to noise . . . . .	12
2.4 Theoretical expectations . . . . .	12
2.4.1 Toy Model . . . . .	15
2.5 Sky background . . . . .	16
2.5.1 Number of apertures and aperture radius . . . . .	17
2.5.2 Sigma clipping . . . . .	19
2.5.3 Combining data sets . . . . .	20
2.6 Potential contrast . . . . .	22
<b>3 Results &amp; Discussion</b>	<b>25</b>
3.1 Stacked frames . . . . .	25
3.2 Simple ADI . . . . .	27
3.2.1 Median . . . . .	31
3.2.2 Flipped Derotation . . . . .	32

## CONTENTS

---

3.2.3	Frame clipping . . . . .	33
<b>4</b>	<b>Summary</b>	<b>37</b>
4.1	Contrast limit - Method comparison . . . . .	37
4.1.1	Size and number of apertures . . . . .	38
4.1.2	Toy model . . . . .	38
4.1.3	Exposure time / Stacked frames . . . . .	39
4.1.4	Simple ADI / Frame selection . . . . .	41
4.1.5	Noise distribution . . . . .	42
4.2	Contrast limit - Comparison to published measured and modeled data . . . . .	43
4.2.1	HR 8799 b . . . . .	45
4.2.2	HR 8799 c . . . . .	46
4.2.3	HR 8799 d . . . . .	47
4.2.4	HR 8799 e . . . . .	48
4.3	Outlook . . . . .	48
	<b>Bibliography</b>	<b>51</b>

---

## List of Figures

---

1.1	Flux of HR 8799 in the long I band with rising aperture radius. . .	2
2.1	Interpolation of the positions for the HR 8799 exoplanets on the 13th of July 2018. . . . .	10
2.2	Background apertures and (brighter) exoplanet apertures for the HR 8799 system. . . . .	11
2.3	Theoretical $S/N$ for a single $t = 120$ s exposure at different aperture radii; $C = 10^{-6}$ , $\beta_{px} = 100$ ; Dashed line $t = 60$ s exposure. . .	13
2.4	Individual noise contributions with respect to separation, aperture radius and exposure time. . . . .	14
2.5	Theoretical $S/N$ for longer exposure times at a fixed aperture radius of $r = 7$ px, $C = 10^{-6}$ , $\beta_{px} = 100$ ; Solid line with individual frames of $t = 120$ s; Dashed line $t = 60$ s. . . . .	15
2.6	Toy model based on data set 120A, camera 1. . . . .	15
2.7	Average count per pixel at different separation to the host star. Data sets: 60X, camera 1 and 120A, camera 1, both derotated. . .	16
2.8	Standard deviation per aperture $\sigma_x$ with respect to different number of apertures, aperture radii and separation to the host star. Data set: 60X, camera 1. . . . .	18
2.9	Localization of clipped apertures ( $> 3\sigma_x$ ) along static PSF spyders ("not derotated"); Exoplanet positions according to north up and east to the left ("derotated"). . . . .	19
2.10	Impact of stacked frames and sigma clipping on $\sigma_x$ ; Data set: 120A, camera 1 Dashed lines and cross mark the data with sigma clipping applied; 40 apertures with $r = 4$ px applied. . . . .	20
2.11	Comparison of data sets 120A and 120B; 40 apertures with $r = 4$ px applied Dashed lines and crosses mark the data with sigma clipping applied. . . . .	21
2.12	Combined derotated and averaged data sets and their impact on $\sigma_x$ . Dotted lines for the data sets with both cameras stacked; 40 apertures with $r = 4$ px applied. . . . .	21

---

LIST OF FIGURES

2.13	Potential $S/N$ and contrast; Data set 60X, camera 1 Dashed lines mark the data with sigma clipping applied. . . . .	22
3.1	$S/N$ for the HR 8799 exoplanets, all data sets stacked and averaged. . . . .	26
3.2	Background, mean flux and exoplanet position flux, all data sets stacked and averaged; $m = 40$ . . . . .	26
3.3	Simple ADI applied to non-derotated data sets. Subtraction of mean and derotation in the aftermath. . . . .	27
3.4	Derotated and subtracted data in logarithmic scale. . . . .	28
3.5	Exoplanet apertures (brightest), background apertures and search grid on simple ADI reduced data. Data sets 60X+120A, both cameras. . . . .	29
3.6	Noise maps of data set 60X, HR 8799 c. . . . .	30
3.7	Simple ADI with median subtraction for all data sets stacked. . . . .	31
3.8	FLIPPED Simple ADI applied to non-derotated data sets. Subtraction of mean and derotation in the aftermath. . . . .	32
3.9	FLIPPED, derotated and subtracted data in logarithmic scale. . . . .	33
3.10	Exoplanet aperture, background apertures and search grid on selected frames, simple ADI reduced data for HR 8799 c. Data sets 120A + 60X, both cameras. . . . .	34
4.1	Our contrast limits for the toy model at a $S/N = 3$ . The toy model is based on data set 120A, camera 1 (dashed line based on data set 60X, camera 1 factorized for a single $t = 120$ s exposure). . . . .	39
4.2	Our Contrast limits for the individual, averaged and derotated data sets at a $S/N = 3$ . Solid lines: Data set camera 1; Dashed lines: Data set camera 2; Toy model factored by $\frac{1}{\sqrt{n_i}}$ . . . . .	40
4.3	Our contrast limits for the individual and combined data sets (averaged and derotated; both cameras). Toy model factored by $\frac{1}{\sqrt{n_i}}$ ; $n_i = 200$ . . . . .	40
4.4	Our contrast limits for simple ADI reduced data sets. Toy model factored by $\frac{1}{\sqrt{n_i}}$ ; $n_i = 200$ Solid lines: mean subtraction; Dashed lines: median subtraction. . . . .	41
4.5	Q-Q-Plots for the aperture flux measurements of the background apertures for HR 8799 c. 40 apertures, $r = 5$ px. . . . .	42
4.6	Measured and modeled contrasts and contrast limits - HR 8799 b. . . . .	45
4.7	Noise map of HR 8799 b - Data set 60X, simple ADI, median subtraction. . . . .	46
4.8	Measured and modeled contrasts and contrast limits - HR 8799 c. . . . .	47
4.9	Measured and modeled contrasts and contrast limits - HR 8799 d. . . . .	47
4.10	Measured and modeled contrasts and contrast limits - HR 8799 e. . . . .	48

---

## List of Tables

---

2.1	Atmospheric conditions during observation (start-end) . . . . .	8
2.2	Astrometry data of HR 8799 b, c, d and e used for the interpolation of the exoplanet positions. . . . .	9
2.3	Interpolated positions of the exoplanets HR 8799 b, c, d and e for the 13th of July 2018. . . . .	9
3.1	$S/N$ for different data sets, when applying a simple ADI. 40 apertures with $r = 4$ px. . . . .	28
3.2	$S/N$ for different data sets, when applying a simple ADI and search grids. 30 apertures with $r = 7$ px. . . . .	30
3.3	$S/N$ for different data sets, when applying a simple ADI with median subtraction. 30 apertures with $r = 7$ px. . . . .	31
3.4	Standard deviation $\sigma_x$ (counts) comparison for differently applied derotations and subtractions. Data sets 120A+60X, 40 apertures with $r = 5$ px. . . . .	32
3.5	$S/N$ for selected frames of the data sets; simple ADI with mean subtraction applied. 40 apertures with $r = 5$ px. . . . .	34
4.1	$\sigma_x$ (counts) of the toy model ( $t = 120$ s) analysis based on different data sets; 40 apertures with $r = 5$ px. . . . .	38
4.2	$f_{mean}$ (counts) of the toy model ( $t = 120$ s) analysis based on different data sets; 40 apertures with $r = 5$ px. . . . .	38
4.3	Applied synthetic absolute flux $F_\lambda$ of the host star HR 8799 based on the ATLAS9 model. . . . .	43



## Chapter 1

---

# Introduction

---

The HR 8799 system was the first directly imaged system of exoplanets. These first detections of direct exoplanet signals from HR 8799 were based on observations by the Keck and Gemini telescopes in the near-IR band ( $1.1 - 4.2\mu\text{m}$ ) [Marois et al., 2008]. The exoplanets HR 8799 b, c and d were confirmed by this analysis. Only two years later a fourth exoplanet, HR 8799 e, was detected with the direct imaging method [Marois et al., 2010].

After the first indirect detections of exoplanets in the 1990's and many follow up studies, constraints were extracted from the available data regarding the masses, orbits and radii of the detected exoplanets. These constraints were dependent on the method used, to detect the respective exoplanet. The ability to detect the emitted light of these exoplanets directly, would further permit to analyze their atmospheres and other physical properties. Due to the refraction of the PSF and the stronger background emission close to the host star, it is easier to detect planets at larger separation. This is contrary to the RV and transit methods, which have a detection bias towards small separation. Therefore exoplanets at larger separation could be found.

The main focus of direct imaging is in the near-IR band. There the contrast of the exoplanet emission with respect to the host star emission is expected to be highest, due to the difference in emission temperatures  $T_{\text{eff}}$  of the objects. In order to analyze more of the SED of the imaged exoplanets and therefore better limit physical properties like  $T_{\text{eff}}$ , the observation of the HR 8799 system in the long I band ( $\lambda = 871\text{ nm}, \Delta\lambda = 56\text{ nm}$ ) was performed with the SPHERE/ZIMPOL instrument at the VLT. A first analysis of the data allowed no confirmation of any of the planets in the long I band. In this master thesis the data is analyzed once more with enhanced astrometry data revealed since. The thesis shall also determine the contrast limits

## 1. INTRODUCTION

---

of the analyzed observations with the applied methods.

### 1.1 Stellar properties of HR 8799

The star HR 8799 is identified in the Henry-Draper catalogue as HD 218396. It is situated at a distance of  $41.29 \pm 0.15$  pc from earth [Wahhaj et al., 2021]. HR 8799 is part of the Columba moving group [Wang et al., 2018]. This star group is estimated to have formed approximately 40 Myr ago. HR 8799 is therefore a young star. It is a main sequence A5 spectral type star [Marois et al., 2008] orbited by at least 4 young, still contracting and therefore self-emitting exoplanets. The exoplanets are situated at ca. 15, 27, 43, and 68 au separation to their host star [Marois et al., 2008].

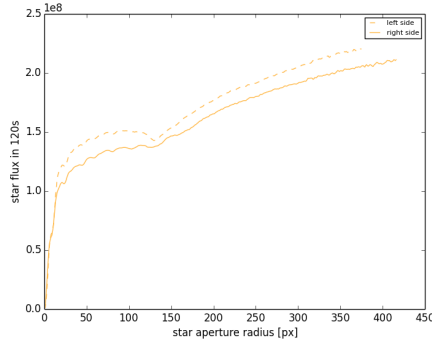


Figure 1.1: Flux of HR 8799 in the long I band with rising aperture radius.

In figure 1.1 you can see the change of intensity of HR 8799 in the long I band, with rising aperture radius. The observation was done by moving the star away from the coronagraph every 20 minutes for a short term integration (1.1s). The data was corrected by the time integration factor to match the count flux of the 120s exoplanet observations.

In order to be able to extend the radial profile up to 416 px, we applied only half apertures. This method was used, as the right side half aperture was observed for all radii up to 416 px. Due to the star being asymmetrically shifted away from the coronagraph for this observation, the left half of the aperture was cut by the imager edge and therefore only integrated up to 375 px. The obtained half fluxes were doubled to extract the left side and right side radial profile.

For all flux determinations (exoplanet and star) the same method was used. To every aperture radius, a donut shaped background aperture with a radius of  $r_{ap} + 2$  px was applied.  $r_{ap}$  is the aperture radius in pixels. The background flux was then subtracted from the aperture flux:

$$f_{st} = f_{tot} - n_{pix} \beta_{pix} \quad (1.1)$$

In equation 1.1  $f_{st}$  is the star flux,  $f_{tot}$  the total flux of the aperture at a certain aperture radius,  $n_{pix}$  is the number of pixels in the aperture and  $\beta_{pix}$  the mean count per pixel in the background aperture. See section 2.3 for further explanations on the aperture photometry methods applied.

With this method the refraction of the PSF influences the total star flux, as you can see in figure 1.1. At an aperture radius just inside the refraction rings, the subtracted background annulus will lead to a reduction in total star flux compared to smaller separations, where the background is not influenced by these aberrations.

The prominent dip of flux at around  $r_{ap} = 140 \text{ px}$  is due to very strong speckles in this area. The coronagraph which obscures part of the flux of the right side of the observation, dimms this effect. This leads to a lower total flux of the right side radial profile, as part of the PSF is blocked by the coronagraph. The total flux of the left side is 4.4% higher than the total flux of the right side.

In order to retrieve an exoplanet signal, it must always be set in relation with the star flux retrieved in the section above. It is crucial, to be aware, that only a part of the total flux of the host star contributes to the possible contrast limit. This is especially important, as rather small aperture radii are used to find the exoplanet signals. The aperture sizes applied to star and exoplanet must always be equal. In the next section you can find all applied methods we used, looking for the exoplanet signal in the long I band, as well as the used formula and data.



## Chapter 2

---

# Measurement & Methods

---

This chapter explains the fundamental theory to understand the analysis of the SPHERE/ZIMPOL observations. We start with a quick overview of the involved telescope and instruments. The section provides also an overview of the observing conditions.

The next part is dedicated to the astrometry considered to set the exoplanet positions and the used calculations to approximate the exoplanet positions during the observation.

Then we summarize the methods used for the aperture photometry, as well as the sky background determinations. Some first steps to optimize the standard deviation per aperture  $\sigma_x$  are evaluated.

The chapter concludes with a first estimate for a potential contrast limit, which could be achieved by the methods applied.

### 2.1 SPHERE / ZIMPOL

The SPHERE instrument is observing data of the VLT telescope of ESO. It is a planet finder instrument built to observe Jupiter-sized old (cold) exoplanets at relatively low separation to their host stars [Thalmann et al., 2008]. To achieve this, it uses the large diameter of the VLT (8 m), the extreme AO system SAXO, a stellar coronograph and finally collects the data in a polarization imager. It was used to observe HR 8799 before, for example with the IRDIS camera and an H band filter ( $\lambda=1.625\mu\text{m}$ ) by [Apai et al., 2016]. In that observation all four exoplanets were confirmed by the data. In order to evaluate the SED at lower wavelengths, our observations were taken with the ZIMPOL imaging polarimeter.

## 2. MEASUREMENT & METHODS

---

Before reaching the ZIMPOL imaging polarimeter, the light from the VLT passes a three-mirror field derotator. It is used to align the sky coordinates by a given angle and have a constant field orientation for the whole observation. As it can be deactivated, one can get access to non derotated data. This technique was used for our observations, in order to reduce spyder and other systematical speckle effects. The non derotated pictures add up to a more even background, when they are derotated in the aftermath. With this method lower standard deviation signals for the background evaluation [Thalmann et al., 2008] are achieved (see section 2.1.1 and 2.5).

After passing this part of the telescope, the wavefront is corrected by the extreme adaptive optics system SAXO. The deformable mirror used ( $d = 180\text{ mm}$ ) has  $41 \times 41$  actuators, with a stroke of  $\pm 3.5\mu\text{m}$ . The tip-tilt mirror has a resolution of  $\pm 0.5\text{ mas}$ . The visible (ZIMPOL) and near-IR (IRDIS and IFS) part of the light is separated by dichroic beam splitters. The visible part of the light is then sensed by a Shack-Hartman wavefront sensor (WFS), with  $40 \times 40$  lenslets operating at a temporal sampling frequency of  $1.2\text{ kHz}$ . This allows the global AO loop to operate with a delay below  $1\text{ ms}$  [Thalmann et al., 2008]. The adaptive optics system corrects, for the wavefront distortions induced by the atmosphere, almost in realtime.

There are several half-wave plates and other instruments in the light path, as well as in the ZIMPOL instrument, to correct the light for polarimetric effects, induced by the passed elements of the telescope. The ZIMPOL polarization imager is able to apply several differential methods regarding the polarization of light. This allows for better contrasts, when searching for exoplanets at low separation to their host star [Thalmann et al., 2008]. These methods and instruments are not further discussed in this paper, as the polarization of the light was not taken into account for our methods.

Once the light has passed the instruments correcting the polarization in ZIMPOL, it is divided by a polarizing beamsplitter and focused onto two specialized CCD cameras. The cameras are exposed intermittently and read out according to their exposure. The ZIMPOL works in the V, R and I bands and is optimized for  $\lambda = 600 - 900\text{ nm}$ .

### 2.1.1 Angular differential imaging (ADI)

As already touched above, the method of angular differential imaging allows to suppress the aberrations, caused by the instruments through non-derotation of the observation field.

When the earth spins below the observed sky, the surrounding of a tracked star spins on the night sky. If the derotator is deactivated, the objects sur-

rounding the star (like exoplanets, or radial apertures) spin around the star in the field of view of the telescope. The instrument aberrations in contrary stay fixed. If the pictures are derotated in the aftermath, the extracted picture shows an average of the aberrations spread around the star. The average noise is therefore reduced, but the exoplanet signal added up on all considered exposures.

To further improve the method, one can subtract the mean or median of a data set from the single data frames before derotation. As the planet moves radially around the star, only a small portion of the planet emission is found in this averaged mean data, "smeared out" over the derotation angle. If we subtract the mean or median from the single exposure frames, the strong aberration features like telescope spyder etc. are reduced systematically, while the exoplanet signal is reduced by a fraction of it's emission only.

### 2.1.2 Observed data properties

The data used in this paper was observed in the nights of the 13th and 14th of July 2018. Observation start on the 13th of July was at 06:40 UTC for the first exposure set. 20 pictures with an exposure of  $t = 120\text{ s}$  were taken by both cameras. This data set is designated in the rest of the paper as set 120A (camera 1 or camera 2 respectively). The number of pictures is designated as number of integrations  $n_i$ . The second set of observations started at 08:23 UTC and again took 20 pictures with an exposure time of  $t = 120\text{ s}$  for each picture (data set 120B). A coronagraph was used for all observations. Unfortunately it was not centered perfectly on the star for the data set 120B. This led to an asymmetric PSF, which made this data set hard to use. In the second night (14th of July 2018) there was an observation of 120 pictures with an exposure time of  $t = 60\text{ s}$  to both cameras (data set 60X). It started at 07:33 UTC. So we have

$$t = 120\text{ s}; n_{i,120} = 20$$

for data sets 120A and 120B; both cameras,

$$t = 60\text{ s}; n_{i,60} = 120$$

for data set 60X; both cameras.

The cameras both take pictures of 512 rows with 1024 pixels. Two rows are separated by a masked row. In order to convert this format to the obtained 1024x1024 pixel data, linearly interpolated rows where inserted between the measured data rows [Schmid et al., 2018]. Pupil stabilized imaging was performed. The filter applied was filter  $I_L$  at  $\lambda = 871\text{ nm}, \Delta\lambda = 56\text{ nm}$ . For

## 2. MEASUREMENT & METHODS

---

more properties of the filter see [Schmid et al., 2018].

The telescope was pointed at the star HR 8799, RA=23:07:28.6; DEC= 21:08:02.3 (J2000) and guided for the observation. As mentioned before the derotation was turned off for the observations.

The star data were retrieved in a short exposure observation without coronagraph on the 13th of July 2018 at 06:35 UTC (shortly before the first set of observations). The exposure time was 1.1 s.

The air mass, seeing, ambient pressure, temperature and wind conditions of the different data sets can be found in table 2.1

Data set	120A (13.7.2018)	120B (13.7.2018)	60X (14.7.2018)
Air mass	1.642-1.625	1.434-1.434	1.475-1.468
Seeing [arcsec]	0.54-0.58	0.66-0.69	0.60-0.56
Wind [deg, $\frac{m}{s}$ ]	0.5, 0.6	52.5, 0.7	204, 1.48
Average $\tau_0$ [s]	0.0080	0.0078	0.0101
Ambient press. [hPa]	746.28-746.28	745.80-745.78	744.97-744.92
Temperature [ $^{\circ}\text{C}$ ]	14.17	14.06	14.04

Table 2.1: Atmospheric conditions during observation (start-end).

## 2.2 Astrometry

The HR 8799 system is a well studied system. The star HR 8799 is situated at RA  $\simeq$  92.76; DEC  $\simeq$  –35.58 in galactic coordinates (ep=J2000) [Universite de Strasbourg/CNRS, 2021]. For our calculations of the astrometric positions of the four exoplanets several astrometric data sets were considered. The aim was to find precise data close to our observation date, the 13th of July 2018.

The closest and most precise determination was found for the innermost planet HR 8799 e. The astrometric evaluation by the GRAVITY Collaboration [Lacour et al., 2019] was done for the 28th of August 2018, only 6 weeks past the observation of our data. [de Rosa et al., 2020] published in 2020 a broad revision of the astrometric calibration of the Gemini Planet Imager (GPI) data. It contained several data points for the HR 8799 exoplanets, which were considered before the revision by [Wang et al., 2018]. [Wahhaj et al., 2021] published astrometric data for the 31st of October 2019, which allowed interpolation of the exoplanet positions for HR 8799 b, c and d. The used data points for the interpolation are collected in table 2.2.

## 2.2. Astrometry

Date	Exoplanet	RA [px]	DEC [px]	Publication
12.09.2014	HR 8799 b	$435.7 \pm 0.9$	$197 \pm 1.2$	[de Rosa et al., 2020]
19.09.2016	HR 8799 c	$-129.4 \pm 0.7$	$229.30 \pm 0.5$	[de Rosa et al., 2020]
19.09.2016	HR 8799 d	$-125.9 \pm 0.5$	$-139.5 \pm 0.5$	[de Rosa et al., 2020]
19.09.2016	HR 8799 e	$-104.5 \pm 0.5$	$22.5 \pm 0.5$	[de Rosa et al., 2020]
28.08.2018	HR 8799 e	$-99.3 \pm 0.1$	$45.6 \pm 0.1$	GRAVITY [Lacour et al., 2019]
31.10.2019	HR 8799 b	$446 \pm 1$	$171.8 \pm 0.5$	[Wahhaj et al., 2021]
31.10.2019	HR 8799 c	$-108.8 \pm 0.4$	$244.1 \pm 0.8$	[Wahhaj et al., 2021]
31.10.2019	HR 8799 d	$-148.9 \pm 0.9$	$-119.6 \pm 0.7$	[Wahhaj et al., 2021]

Table 2.2: Astrometry data of HR 8799 b, c, d and e used for the interpolation of the exoplanet positions.

The interpolations were done by interpolating the radius as well as the angle of the known astrometric data closest to the observation for HR 8799 b, c and d. For HR 8799 e the RA and DEC data were interpolated, since the astrometry by [Lacour et al., 2019] was RA and DEC data. The precision of the interpolation regarding the time was  $\pm$  one day. All data was converted into RA and DEC deviation in pixels with respect to the host star HR 8799 for the SPHERE/ZIMPOL instrument. One pixel corresponds approximately to 3.60 mas in x-direction (RA) and 3.62 mas in y-direction (DEC) [Schmid et al., 2018]. The errors were propagated accordingly. The derived interpolated positions of the exoplanets for our observations are shown in table 2.3.

Exoplanet	RA [px]	DEC [px]	$\rho$ [mas]	PA [deg]
HR 8799 b	$444 \pm 1.1$	$178 \pm 2$	$1721 \pm 3.1$	$68.2 \pm 0.3$
HR 8799 c	$-118 \pm 1$	$238.2 \pm 0.7$	$952 \pm 1.9$	$333.6 \pm 0.3$
HR 8799 d	$-139.6 \pm 0.8$	$-128.4 \pm 0.8$	$681 \pm 2.4$	$227.6 \pm 0.3$
HR 8799 e	$-99.7 \pm 0.1$	$43.6 \pm 0.2$	$392.2 \pm 0.8$ <sup>1</sup>	$293.76 \pm 0.04$ <sup>1</sup>

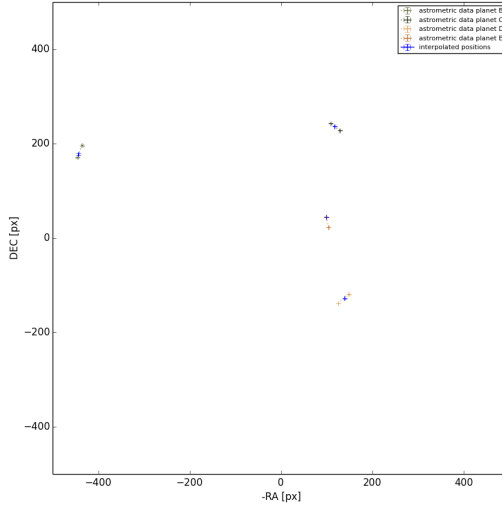
Table 2.3: Interpolated positions of the exoplanets HR 8799 b, c, d and e for the 13th of July 2018.

On the next page in figure 2.1 you can find a visualization with the detailed data positions and interpolation positions for all four exoplanets. You can see that the interpolated positions are displaced from the direct lines between the data points. This displacement is due to the radial movement of the exoplanets and the used radial and angular data to interpolate the positions of the exoplanets.

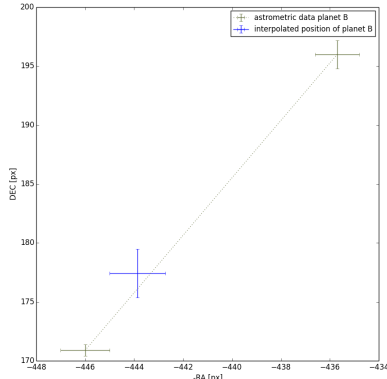
<sup>1</sup>The interpolated position of exoplanet HR 8799 e was calculated with the RA/DEC positions, as these were the closest and most precise astrometry data available.

## 2. MEASUREMENT & METHODS

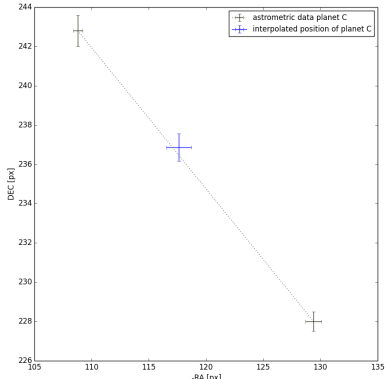
---



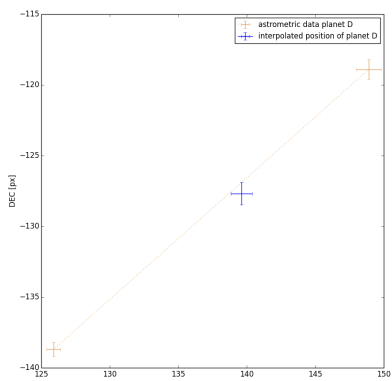
(a) HR 8799 exoplanet system overview of astrometric data points.



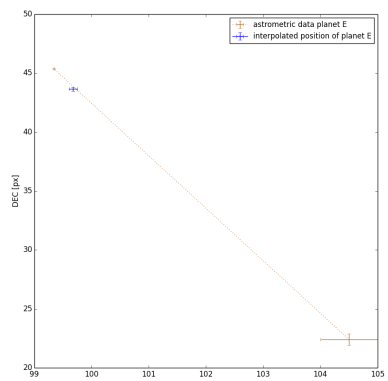
(b) HR 8799 b.



(c) HR 8799 c.



(d) HR 8799 d.



(e) HR 8799 e.

## 2.3 Aperture photometry

In this thesis aperture photometry was used, to extract the flux of the star and the exoplanets from our data. The noise was extracted with a statistic approach. To calculate the background, a set number of apertures with defined shapes and sizes were placed radially at the same distance from the host star as the interpolated exoplanet position (see 2.2 Astrometry). Find an aperture visualization on one of the data frames of our observation in figure 2.2.

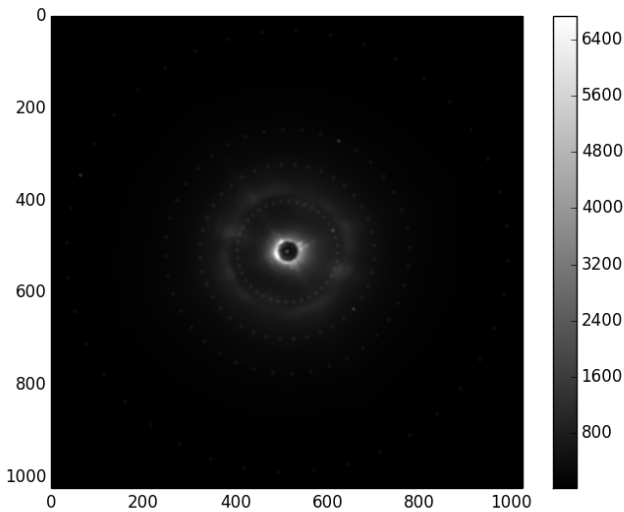


Figure 2.2: Background apertures and (brighter) exoplanet apertures for the HR 8799 system.

All apertures were equipped with an additional donut shaped background aperture surrounding the round apertures, to determine the sky background.

The signal per pixel of such a sky background aperture with  $n$  pixels is:

$$\beta_{px} = \frac{1}{n} \sum_{i=1}^n c_i \quad (2.1)$$

Where  $c_i$  is the signal count of the imager in one pixel.

To get the flux from an aperture with  $n_{px}$  pixels, we have to subtract the sky background from the total aperture signal. Therefore we get:

$$f_{ap} = f_{tot} - n_{px}\beta_{px} \quad (2.2)$$

Where  $f_{tot}$  is the total aperture flux.

## 2. MEASUREMENT & METHODS

---

### 2.3.1 Signal to noise

In order to confirm an exoplanet signal, the  $S/N$  ratio must be higher than the standard deviation of the data set. In order to calculate the  $S/N$  ratio, we used the following formulas:

The target aperture is  $ap = 1$ . With an aperture ring of  $m$  apertures, the mean background flux is determined by:

$$f_{mean} = \frac{\sum_{ap=2}^m f_{ap}}{m - 1} \quad (2.3)$$

Each  $f_{ap}$  is calculated as stated in equation 2.2.

The standard deviation of this mean flux is then:

$$\sigma_x = \sqrt{\frac{1}{m - 2} \sum_{ap=2}^m (f_{ap} - f_{mean})^2} \quad (2.4)$$

and signal to noise is given by:

$$S/N = \left( \frac{f_1 - f_{mean}}{\sigma_x} \right) \quad (2.5)$$

You can find a more detailed description of aperture photometry and all the formulas used in this section in [Howell, 1989].

## 2.4 Theoretical expectations

When we analyze an aperture photometry for it's theoretical  $S/N$ , we apply the following formula:

$$S/N = \frac{f_\gamma}{\sqrt{f_\gamma + n_{px}\beta_\gamma + E_{read}^2 n_{px}}} \sqrt{n_i} \quad (2.6)$$

The time factor is given in our 120A and 120B data sets by  $t = 120$  s for one integration and already factored into our variables.  $n_i$  is the number of 120s frame integrations. A similar approach can be taken for the 60X data set. Here the variables are defined for a  $t = 60$  s. An equal  $n_i$  results therefore in half the total exposure time for this data set. See section 2.1.2 for more information on the observations.

For the noise we have several contributions:

## 2.4. Theoretical expectations

---

- Photon noise:  $f_\gamma$  is the theoretical exoplanet signal (at an exposure of  $t = 120$  s) multiplied by the CCD gain of  $10.5 e^-/\text{ADU}$ , so

$$f_\gamma = 10.5 f_1$$

$f_1$  is the exoplanet aperture flux in counts, as derived in equation 2.2. It is extracted from the star flux for a certain aperture radius  $r$ . The square root of this signal determines the photon noise.

- Background noise: The background noise is given by our background signal/pixel  $\beta_{px}$  (at an exposure of  $t = 120$  s; see equation 2.1) again multiplied by the CCD gain. Therefore the background noise per pixel is

$$\beta_\gamma = 10.5 \beta_{px}$$

To get the total noise contribution, we have to factor it by the number of aperture pixels  $n_{px}$ . This sets the background noise.

- Readout noise:  $E_{read}$  is the noise per integration (number of integrations  $n_i$ ) and aperture pixel ( $n_{px}$ ) for a single read out process. For the ZIMPOL instrument the CCD gain is  $10.5 e^-/\text{ADU}$  (detector counts) and the read-out noise  $N_{ron} = 2 \text{ ADU/frame}$  and aperture pixel. Therefore

$$E_{read} = 10.5 \cdot 2 = 21$$

To get the read out noise of one integration  $E_{read}$  has to be factored by the number of pixels  $n_{px}$ .

Dark noise is not considered for our data, since it has a too small contribution.

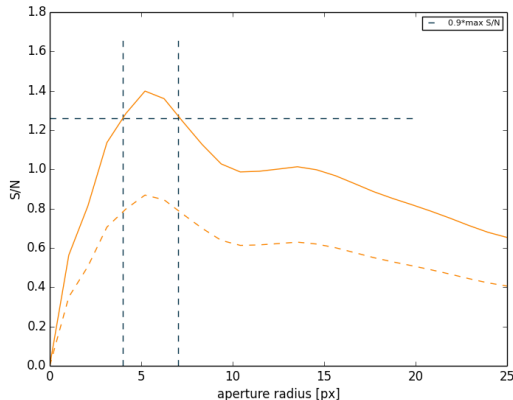


Figure 2.3: Theoretical  $S/N$  for a single  $t = 120$  s exposure at different aperture radii;  $C = 10^{-6}$ ,  $\beta_{px} = 100$ ; Dashed line  $t = 60$  s exposure.

## 2. MEASUREMENT & METHODS

---

For a theoretical exoplanet signal at a contrast of  $C = 10^{-6}$  (upper limit, see section 4.2 for more details) of the measured starflux signal (see equation 2.7) and a background noise count of  $\beta_{px} = 100$  (approximately exoplanet HR 8799 c see section 2.5) this yields the  $S/N$  curve as shown in figure 2.3 for different aperture radii.

The maximal  $S/N$  is reached at  $r = 5$  px. At bigger aperture radii the background contribution is getting larger in relation to the gain in signal. At  $r \in [4, 7]$  px, a minimum of 90 % of the maximal  $S/N$  is achieved. For our analysis, we allowed aperture radii in this span.

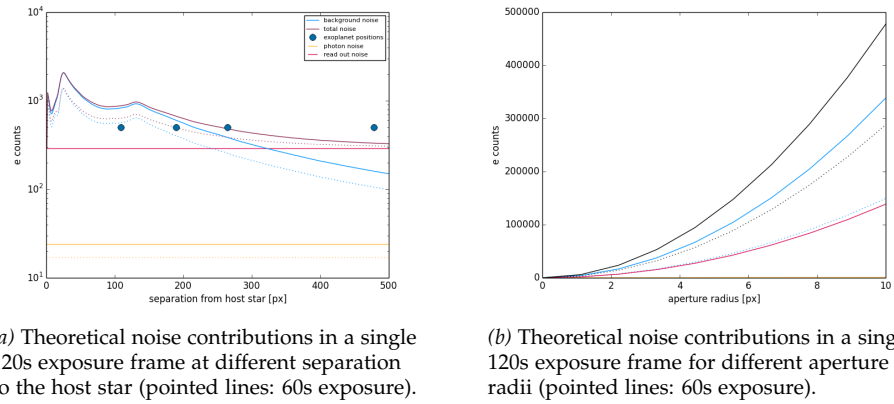


*Figure 2.4:* Individual noise contributions with respect to separation, aperture radius and exposure time.

In figure 2.4a you see the different regimes of dominant noise contribution. For HR 8799 e and HR 8799 d, background noise is dominant. For HR 8799 c we have a mix of background and read out noise contributing most to the total theoretical noise. Further out the region of HR 8799 b is dominated by read out noise. As the read out noise is the same for a 60s and 120s exposure, this rises the total noise with respect to a signal for the 60s exposures in this area. For a detection of HR 8799 b, but also for HR 8799 c longer exposure times for the individual frames would be favorable.

All noise contributions grow quadratic with respect to the aperture radius (see figure 2.4b), as they are proportional to  $n_{px} = \pi r_{ap}^2$ . All noise factors combined should lead to the statistical noise in our data. We have to keep in mind, that the theoretical frame work and our statistical data analysis are done in two different regimes.

## 2.4. Theoretical expectations

---

The theoretical gain for  $S/N$  at longer exposure is found in figure 2.5.

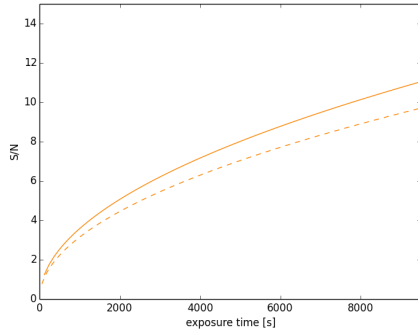


Figure 2.5: Theoretical  $S/N$  for longer exposure times at a fixed aperture radius of  $r = 7$  px,  $C = 10^{-6}$ ,  $\beta_{px} = 100$ ; Solid line with individual frames of  $t = 120$  s; Dashed line  $t = 60$  s.

### 2.4.1 Toy Model

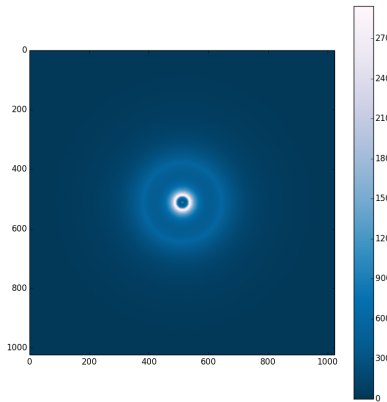


Figure 2.6: Toy model based on data set 120A, camera 1.

In order to be able to compare our analysis to a gaussian normal distribution, we applied a toy model with a normal distributed noise along the PSF. The PSF was extracted from the averaged, derotated data sets 120A, camera 1 and 60X, camera 1.

For every radius an average signal was computed from the data set. This signal was used as the mean for a random noise distribution along the same

## 2. MEASUREMENT & METHODS

---

radius, with a normal standard deviation based on the theoretical noise values (see section 2.4). Find the toy model for data set 120A, camera 1 in figure 2.6.

### 2.5 Sky background

Due to the shape and refractions of the PSF, the sky background has a different sensitivity, dependent on the separation from the star. In general the total counts diminish with radius, but as you can see in figure 2.7, there are regions of enhanced aberrations, which have a lower sensitivity than their surroundings. The innermost radii are covered by the coronagraph.

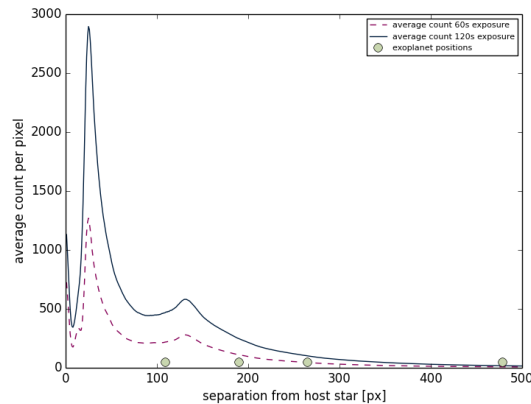


Figure 2.7: Average count per pixel at different separation to the host star.  
Data sets: 60X, camera 1 and 120A, camera 1, both derotated.

As HR 8799 b was measured at a significantly lower emission than the other three exoplanets in the IR band by [Marois et al., 2008], HR 8799 c is the most promising candidate to be revealed regarding the sensitivity of the sky background. It is placed outside the most prominent aberration features.

One has to take into account though, that the reflection of the host star light of HR 8799 b can be just as strong as the one of the other planets. This contributes more to the emission of the exoplanet in the I band, than in the IR. As the IR emission of the exoplanets is influenced by their contraction and therefore self-emission, it is only a hint for the emission of the respective exoplanet in the I band

### 2.5.1 Number of apertures and aperture radius

As we considered a statistical approach to analyze our data, we were especially interested in the standard deviation of the mean aperture flux  $\sigma_x$ . To minimize  $\sigma_x$  and therefore maximize  $S/N$ , the number of apertures as well as their size was investigated. An aperture smaller than a radius of 2 px was not considered, in order to have a reasonable chance of detecting the exoplanet signal within an aperture and as the positioning error of the host star is already at  $\pm 1$  px.

Especially for the two innermost planets the apertures begin to overlap, when adding apertures. For an aperture radius of 5 px (sky background radius 7 px), the overlap starts with 48 apertures for HR 8799 e, 85 apertures for HR 8799 d, 118 apertures for HR 8799 c and 215 apertures for HR 8799 b. For an aperture radius of 2 px (sky background radius 4 px), the overlap starts with 84 apertures for HR 8799 e, 148 apertures for HR 8799 d, 205 apertures for HR 8799 c and 376 apertures for HR 8799 b. Therefore we considered a maximum of 40 radially symmetric placed apertures at the same separation to the star as the exoplanet signal.

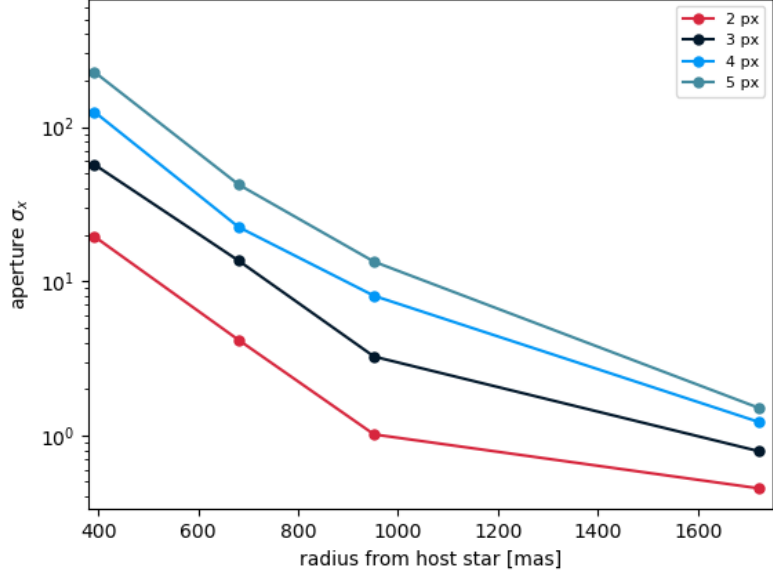
As you can see in figure 2.8a, the standard deviation gets lower, if you move away from the star. This is in alignment with lower total counts at high separation to the host star, as seen in figure 2.7.

If we have a closer look at the different exoplanets, we can see, that the number of apertures has only a marginal influence on  $\sigma_x$ . Especially for longtime exposed derotated pictures, the gain of evaluating more apertures is negligible. This is due to the fact, that with this method the aberration features are smoothed (as explained in section 2.1.1), as the data is already averaged over many exposures.

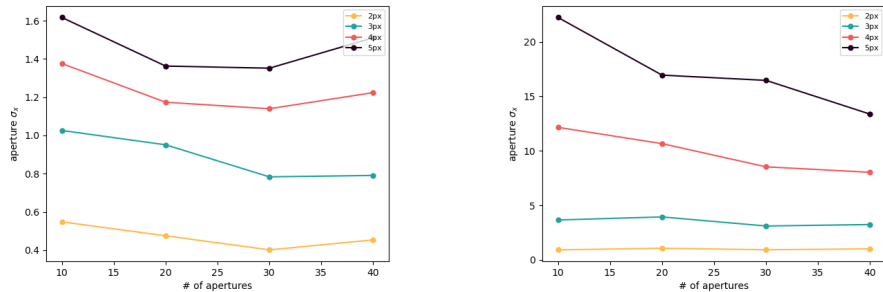
The rise of  $\sigma_x$  with larger aperture radii is, as expected, significant, as it is a standard deviation with respect to an aperture mean flux  $f_{mean}$ . As a larger aperture radius is also enhancing the abundance of the exoplanet signal, the ratio of the two values has to be optimized, as shown in section 2.4.

## 2. MEASUREMENT & METHODS

---

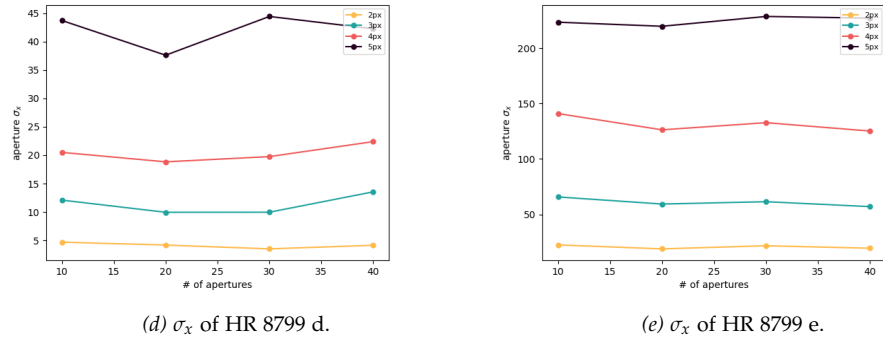


(a) Standard deviation  $\sigma_x$  of the aperture signal with 40 apertures at the different separations of the exoplanets to the host star.



(b)  $\sigma_x$  of HR 8799 b.

(c)  $\sigma_x$  of HR 8799 c.



(d)  $\sigma_x$  of HR 8799 d.

(e)  $\sigma_x$  of HR 8799 e.

Figure 2.8: Standard deviation per aperture  $\sigma_x$  with respect to different number of apertures, aperture radii and separation to the host star. Data set: 60X, camera 1.

### 2.5.2 Sigma clipping

To enhance  $\sigma_x$  further, we applied a filter to the individual aperture signals. All apertures with more than  $3\sigma_x$  were clipped. In figure 2.9 you can see, that the canceled apertures are in general close to the main aberration features. For this evaluation the individual exposures of data set 120A were

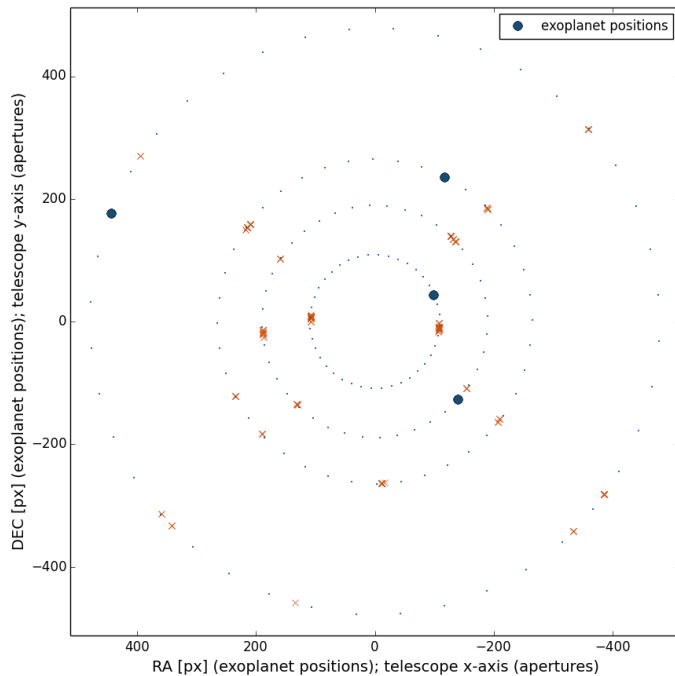


Figure 2.9: Localization of clipped apertures ( $> 3\sigma_x$ ) along static PSF spyders ("not derotated"); Exoplanet positions according to north up and east to the left ("derotated").

analyzed. To keep the standard deviation comparable, we always averaged the data when adding frames, such that we had averaged 120 s exposures after the sum up. You can see in figure 2.10a, that  $\sigma_x$  is lowered for the averaged summed up frames. This is more pronounced for exoplanet HR 8799 b far away from the refraction ring of the PSF. For all exoplanets a better  $\sigma_x$  is achieved, when applying the  $3\sigma_x$  clipping.

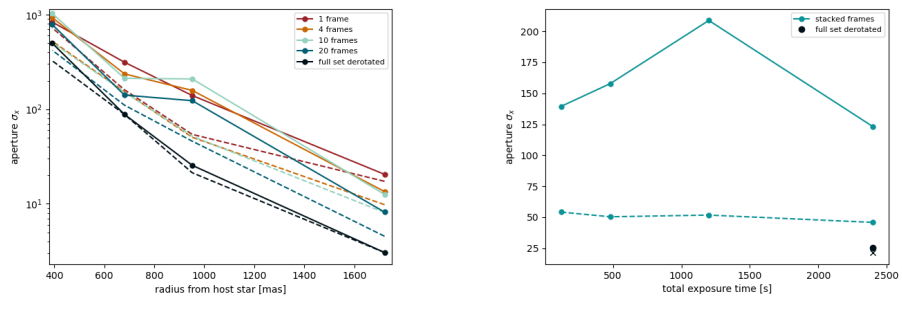
The derotated data outperforms the added frames, when it comes to  $\sigma_x$  though. This is due to the smoothening effect on single speckles, when applying the derotation in the aftermath of the data collection (see section 2.1.1). Without the applied derotation the prominent aberration features and

## 2. MEASUREMENT & METHODS

---

speckles of the optical effects dominate the statistics.

If we have a closer look at the values of HR 8799 c, you can see in figure 2.10b, that for this data set the lowering of  $\sigma_x$  is insignificant, when adding more observation frames. The  $\sigma_x$  clipping is balancing negative effects in single frames. The lowest values are achieved with the derotation method. The effectiveness of this method is also reflected by the fact, that almost no apertures are clipped in this data set (above the  $3\sigma_x$  threshold).



(a) Adding frames (exposure time) and the impact on  $\sigma_x$ .

(b) Different exposure times (added individual frames) for HR 8799 c and their impact on  $\sigma_x$ .

Figure 2.10: Impact of stacked frames and sigma clipping on  $\sigma_x$ ; Data set: 120A, camera 1  
Dashed lines and cross mark the data with sigma clipping applied; 40 apertures with  $r = 4$  px applied.

### 2.5.3 Combining data sets

In order to maximize the total exposure time of the observation, we tried to combine the entire derotated data sets. All data sets were averaged and derotated before the analysis as explained in section 2.1.1. First we analyzed the different 20 pictures 120 s exposure collections. You can see a comparison of the data sets in figure 2.11a. As expected the standard deviation was worse for the 120B data set, due to the misaligned placement of the coronagraph. In our data this has a strong impact especially at high separation compared to the other data sets. There was a particularly strong aberration feature exactly at the same separation to the star as HR 8799 b in data set 120B, camera 1. The  $\sigma_x$  for HR 8799 c are rather comparable though. See figure 2.11b for a closer look at the  $\sigma_x$  of HR 8799 c.

As the 120B data was acceptable for all exoplanets except HR 8799 b, we included it in the analysis of adding the derotated datasets up and averaging them. In figure 2.12 you can find the results for the standard deviation for the combined data sets.

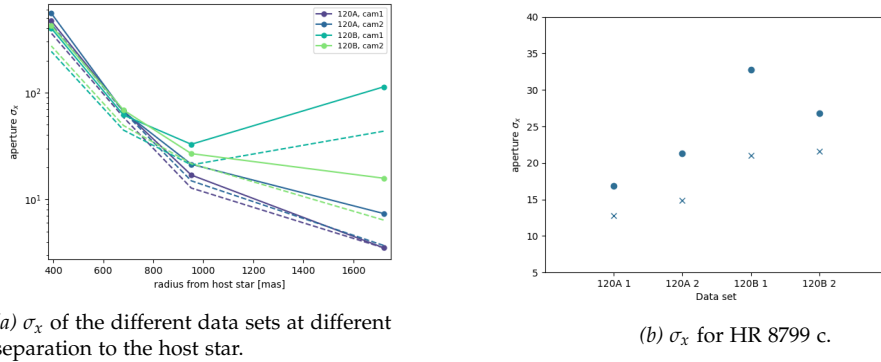


Figure 2.11: Comparison of data sets 120A and 120B; 40 apertures with  $r = 4$  px applied  
Dashed lines and crosses mark the data with sigma clipping applied.

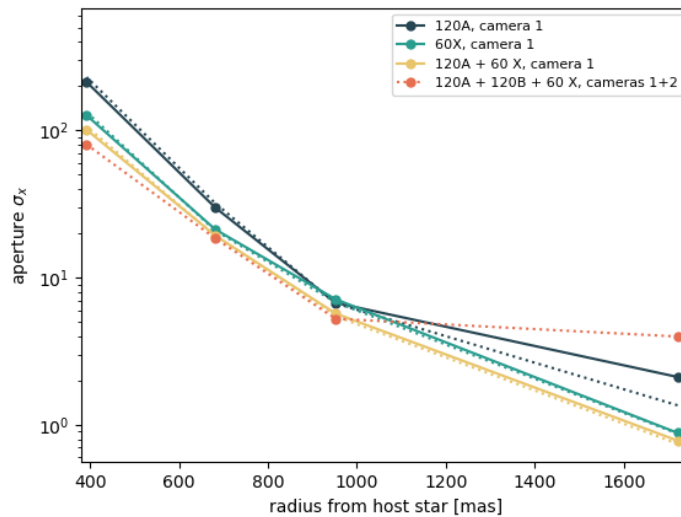


Figure 2.12: Combined derotated and averaged data sets and their impact on  $\sigma_x$ .  
Dotted lines for the data sets with both cameras stacked; 40 apertures with  $r = 4$  px applied.

Except for the outermost exoplanet HR 8799 b, the combination of both cameras has almost no impact on  $\sigma_x$ . This hints at the fact, that the residual  $\sigma_x$  is due to atmospheric or telescope aberrations, as the pictures were taken almost simultaneously.

The combination of all data sets yields a lowering of  $\sigma_x$  with a factor 1.4-2.4 with respect to the 120A, camera 1 data set only. For the S/N this would contribute to an enhancement of factor 1.1-1.4. This too points at optical

## 2. MEASUREMENT & METHODS

---

effects influencing the statistics strongly, as with a 10 times longer total exposure time (total data:  $t = 24\,000\text{ s}$ ), one would expect a  $S/N$  three times higher than the one from data set 120A, camera 1 ( $t = 2400\text{ s}$ ).

### 2.6 Potential contrast

If we simulate an exoplanet signal at a contrast  $C$  with respect to the host star:

$$f_{1,sim} = C \cdot f_{st} \quad (2.7)$$

and apply the methods from section 2.3, the simulated  $S/N$  for the exoplanets in figure 2.13a are obtained. The simulation is based on the extracted  $\sigma_x$  and mean aperture flux  $f_{mean}$  at the respective separation to the host star for 40 apertures; Aperture radius  $r = 4\text{ px}$ ; Data set 60X, camera 1 derotated and averaged.  $f_{st}$  is obtained from the host star exposure away from the coronagraph with the same aperture size and factored for exposure time (see section 1.1, equation 1.1).

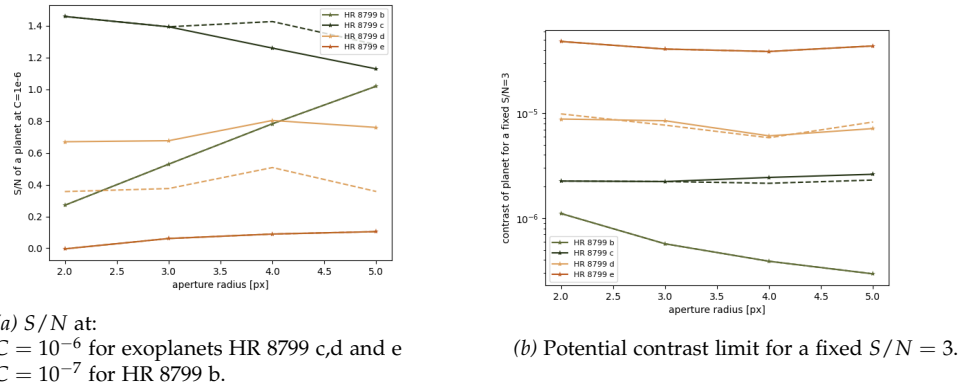


*Figure 2.13: Potential  $S/N$  and contrast; Data set 60X, camera 1  
Dashed lines mark the data with sigma clipping applied.*

As [Marois et al., 2008] measured HR 8799 b at a contrast of  $0.6 \cdot 10^{-5}$  in the near-IR band, which would yield a contrast of  $10^{-7}$  in the visible band, this contrast was applied for the simulation for this planet. The contrast for the other exoplanets was simulated at a rather high  $C = 10^{-6}$ . Find a discussion of the measured and predicted contrasts for the different exoplanets in section 4.2.

The dashed line data are the obtained  $S/N$  for the sigma clipping method (see section 2.5.2). For planet HR 8799 d this yields lower  $S/N$ , as the  $f_{mean}$

is significantly negative for the unclipped data set.

Considering gaussian noise distribution for the statistics and the obtained data, the signal for HR 8799 c is not visible in this data set. The assumed contrast of  $C = 10^{-6}$  is at the high end of predictions (see section 4.2.2 for details of the measured and modeled contrasts for HR 8799 c). Also for the other exoplanets the noise is probably too strong, to be able to find a clear signal in this data set alone.

In figure 2.13b the contrast limits for data set 60X, camera 1 were calculated with a fixed  $S/N = 3$ . The contrast was again with respect to the host star signal at the same aperture radius. All exoplanet separations have a contrast limit above the theoretical contrast in the visible light.

Our data observed by the VLT telescope and imaged by the ZIMPOL instrument was analyzed and framed. From published observations we were able to interpolate and determine our exoplanet positions within our set framework. We also defined the used formulae and structures for our statistical background determinations. A gaussian toy model, based on the PSF sensitivity, was constructed as a reference.

We then analyzed the impact of aperture number and size on our statistics. The exposure time as well as unexpected high deviations in signal from our mean values were checked. Finally we were able to set a first potential contrast limit.

With the methods and formulae fixed for our analysis we now tackle the task to find a possible exoplanet signal.



## Chapter 3

---

# Results & Discussion

---

In order to detect an exoplanet signal, a  $S/N > 3$  (see section 2.3.1) shall be achieved. Considering a Gaussian noise distribution, 99.73% of all values should be within the  $3\sigma$  limit. The low  $S/N$  is therefore acceptable, as the astrometric position of the exoplanets is known to a certain precision from the near-IR observations by [de Rosa et al., 2020], [Lacour et al., 2019] and [Wahhaj et al., 2021]. The aperture  $ap = 1$  is always our target aperture. Its position is determined by the interpolation of the available astrometry data cited above (see section 2.2).

As seen in section 2.5, an aperture ring of more than 40 apertures is making apertures overlap for an aperture radius of  $r = 5$  px at the innermost exoplanet separation. For an aperture radius of  $r = 7$  px this is true for more than 35 apertures. The addition of apertures yields no enhanced  $\sigma_x$  for stacked and averaged data sets as seen in section 2.5.1. We therefore conducted the further analysis within the range of background determination rings of 30-40 apertures.

### 3.1 Stacked frames

In a first try we added all derotated data sets, which were averaged before the analysis. The data sets were combined to a total data set, weighted for their exposure time contribution and reduced to a 60s exposure, so:

$$Maxset60 = 0.4 \left( \frac{\frac{120A_1 + 120A_2 + 120B_1 + 120B_2}{4}}{2} \right) + 0.6 \left( \frac{60X_1 + 60X_2}{2} \right) \quad (3.1)$$

$120A_1$  is the data set 120A, camera 1, the other data sets are labeled correspondingly (see section 2.1.2).

### 3. RESULTS & DISCUSSION

---

The final stacked and averaged frame (Maxset60) was then analyzed, applying aperture rings with 40 apertures to determine the statistical noise as explained in section 2.3. The  $S/N$  obtained, was insignificant for all results (see figure 3.1). If we analyze the contributing factors, we find, that there is

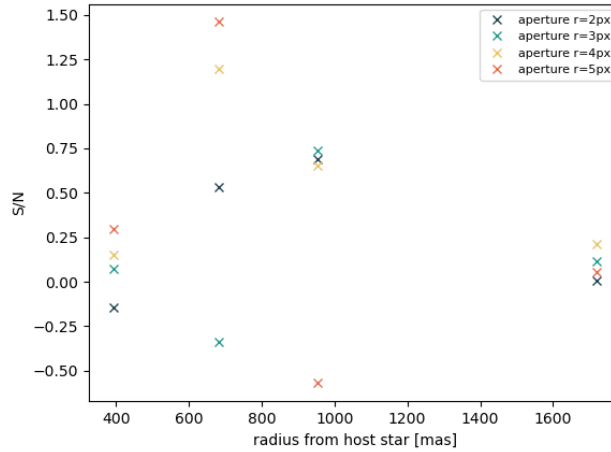
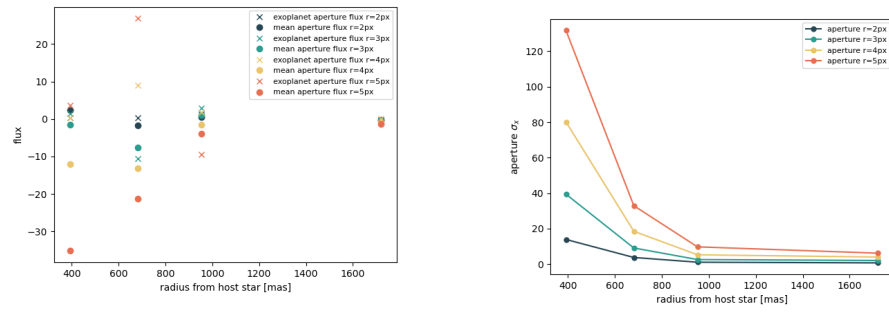


Figure 3.1:  $S/N$  for the HR 8799 exoplanets, all data sets stacked and averaged.

almost no flux in the exoplanet aperture rings and no significant difference to the mean flux of the apertures. Find the flux analysis, as well as the standard deviation in figure 3.2.



(a) Exoplanet position flux and mean flux of the background apertures.

(b)  $\sigma_x$  for the background apertures.

Figure 3.2: Background, mean flux and exoplanet position flux, all data sets stacked and averaged;  $m = 40$ .

With a gaussian noise distribution one could theoretically achieve a  $S/N > 3$

with the stacked and averaged frame (total exposure time  $t = 24\,000$  s, see figure 3.7). As seen in this section, this is not the case. Speckles and other aberration features are dominant in the statistics and alter the noise distribution significantly. Therefore we had to dig deeper into our data.

## 3.2 Simple ADI

In order to get rid of the systematic speckles attributed to spyder and other aberration effects, we applied a simple angular differential imaging (ADI) (see section 2.1.1) subtraction to our data. The non-derotated single exposure frames were subtracted by the mean of the non-derotated data set. This reduced the most prominent speckle features. After the subtraction the single frames were derotated and then averaged before the analysis. The

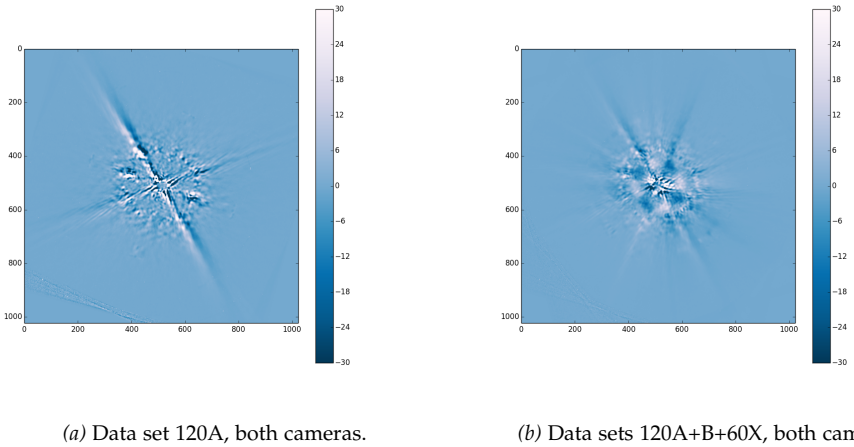


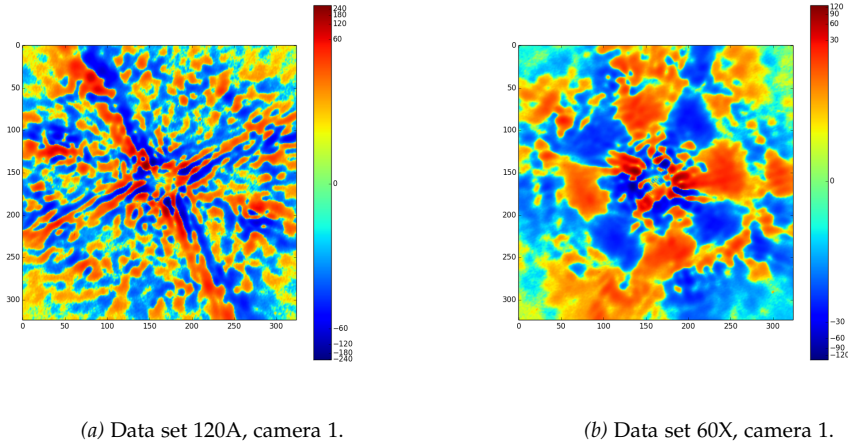
*Figure 3.3:* Simple ADI applied to non-derotated data sets. Subtraction of mean and derotation in the aftermath.

obtained data are seen in figure 3.3. The prominent aberration structures are strongly reduced. The data set 120A was derotated by a total angle of  $10.358^\circ$  between the first and the last exposure frame, corresponding to the sky rotation during the total observation time for this data set. Data set 120B was derotated by  $12.188^\circ$  between the first and the last exposure frame. For the 60s exposures, the total observation time was longer (120 integrations). The data set 60X was derotated by  $44.885^\circ$  between the first and the last exposure frame. In a logarithmic scale for the obtained subtracted and derotated pictures one can clearly see the effect of the derotation angle (see figure 3.4).

A first analysis provided no significant results for any data set. The maximal

### 3. RESULTS & DISCUSSION

---



(a) Data set 120A, camera 1.

(b) Data set 60X, camera 1.

Figure 3.4: Derotated and subtracted data in logarithmic scale.

Data set	HR 8799 b	HR 8799 c	HR 8799 d	HR 8799 e
120A <sub>1</sub>	0.86	0.37	-0.41	-0.74
120A <sub>2</sub>	-1.13	0.43	-0.55	-0.89
120B <sub>1</sub>	-0.21	-0.02	0.81	-0.40
120B <sub>2</sub>	-0.28	-0.65	0.72	-0.92
60X <sub>1</sub>	0.06	2.34	0.54	0.64
60X <sub>2</sub>	-0.17	1.99	1.40	0.37

Table 3.1:  $S/N$  for different data sets, when applying a simple ADI.  
40 apertures with  $r = 4$  px.

$S/N$  achieved was at 2.34, which is within statistics. Considering a Gaussian distribution,  $2.34 \sigma_x$  would be achieved for 1 % of the data only. As we have seen, the speckle and aberration features are influencing the statistics strongly though, so a result like this should at least be confirmed in the other data sets, which is not the case. Find the  $S/N$  data for this analysis in table 3.1

When we take a closer look at the contributing factors, we especially see, that we have almost nowhere a significant exoplanet flux  $f_1$ . As we wanted to further explore the area around our calculated astrometry 2.2, we enlarged our aperture radii to  $r = 7$  px. To provide overlapping of the larger background apertures and since our analysis did not determine significant  $\sigma_x$  dependence on the number of apertures for averaged data sets (see section 2.5.1), we applied aperture rings with  $m = 30$  apertures. We also implemented search grids of  $20 \times 20$  px, to find higher flux areas close to the obtained astrometry (see figure 3.5). This corresponds to an area of approx-

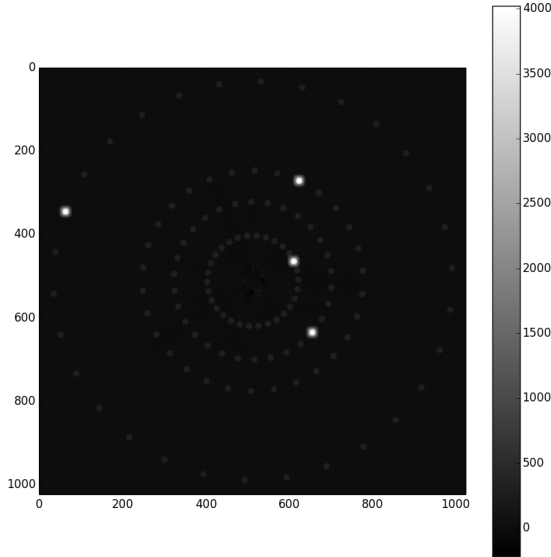


Figure 3.5: Exoplanet apertures (brightest), background apertures and search grid on simple ADI reduced data. Data sets 60X+120A, both cameras.

imately  $72 \times 72$  mas on the night sky.

The data sets 120A and 120B did provide apertures within the grid with a  $S/N > 3$ . As this first analysis was based on the original astrometry background ring and separation for  $f_{mean}$  and  $\sigma_x$ , we now had to apply the new aperture background ring to the offset astrometry. We got enhanced  $S/N$  but still at  $S/N < 3$  (see table 3.2). This showed the high dependence of the background with respect to the separation to the host star. The standard deviation  $\sigma_x$  as well as the mean background flux  $f_{mean}$  were significantly altered even for very small changes in separation to the host star. This effect could also be reproduced with the toy model (see section 2.4.1) and was therefore considered systematical.

Furthermore the  $S/N$  was reduced, when combining both cameras in the offset position, contrary to what one would expect for the longer exposure. When we added the 60X data set, the higher  $S/N$  areas vanished completely, strongly pointing at speckles responsible for the higher flux areas.

For the combined data (both cameras) of set 60X we found a  $S/N = 3.84$  for our astrometry of HR 8799 c. We found in both cameras areas with even higher  $S/N$  close to our astrometry for HR 8799 c. Focusing on these ar-

### 3. RESULTS & DISCUSSION

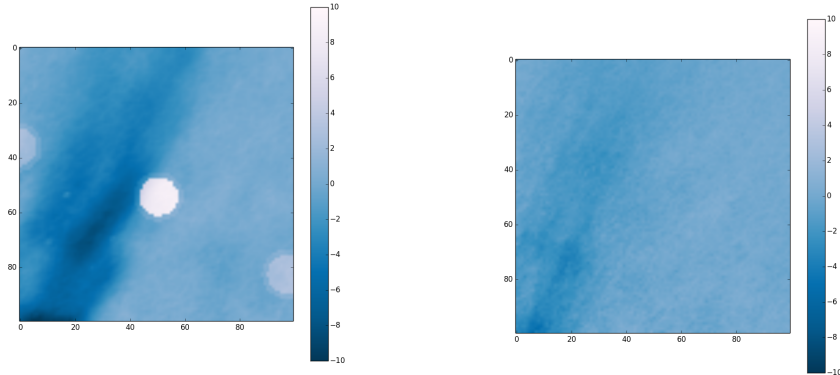
---

eas did not provide an enhanced  $S/N$  (see table 3.2). When combining the data set 60X with data set 120A, we obtained a  $S/N = 4.03$  (offset focus  $S/N = 4.13$ ) . When adding data set 120B though, the  $S/N$  was lowered again.

Data set	HR 8799 b	HR 8799 c	HR 8799 d	HR 8799 e
120A <sub>1</sub>	-1.30	0.44	-0.15	-0.48
120A	-0.34	0.48	-0.21	-0.59
60X	0.28	3.84	0.81	0.20
120A+60X	0.01	4.03	0.51	-0.01
120A+B+60X	-0.44	1.72	1.03	-0.35
60X offset	-0.36	3.80	0.53	-0.93
120A+60X offset	-0.29	4.19	0.55	0.33
120A+B+60X offset	-0.54	1.51	1.42	1.18

Table 3.2:  $S/N$  for different data sets, when applying a simple ADI and search grids. 30 apertures with  $r = 7$  px.

When we have a closer look at the data, we see, that the high  $S/N$  is due to an aberration feature (resulting from a residual telescope spyder) in data set 60X (see figure 3.6). The structure, leading to an add in counts (due to a negative count area in the background aperture), disappears, when we subtract the median of the data set instead of the mean (see next section 3.2.1).



(a) Linear noise map of data set 60X,  
simple ADI with mean subtraction.  
Visualization of apertures.

(b) Linear noise map of data set 60X,  
simple ADI with median subtraction.

Figure 3.6: Noise maps of data set 60X, HR 8799 c.

### 3.2.1 Median

In a next analysis we applied the same method, using the median of the total set to subtract the strong aberration features. The results were within the statistics for all data sets and grids (see table 3.3). There were some areas within the grids of single data sets, which were at  $S/N > 3$ . They vanished, when centering them and adding other data sets, just like with the areas for the mean subtraction.

Data set	HR 8799 b	HR 8799 c	HR 8799 d	HR 8799 e
120A <sub>1</sub>	-1.15	-0.08	0.12	-1.58
120A	-1.23	0.26	0.25	-1.07
60X	-0.37	-0.10	0.09	-0.22
120A +60X	-0.95	0.03	0.22	-0.83
120A+B +60X	-1.20	0.38	1.67	-0.91

Table 3.3:  $S/N$  for different data sets, when applying a simple ADI with median subtraction. 30 apertures with  $r = 7$  px.

As you can see in figure 3.7 the median subtraction further smoothes the aberration features, especially in data set 60X (compare to figure 3.3b). Find a comparison of both methods in section 4.1.4.

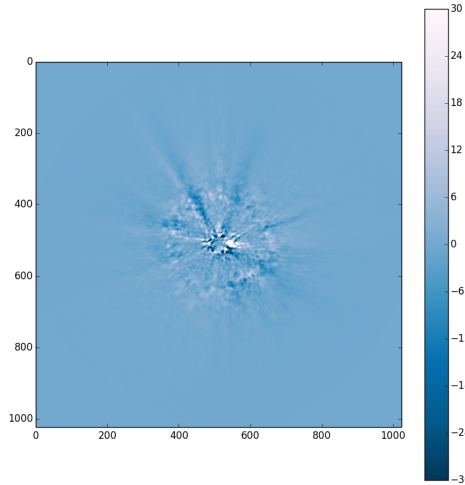


Figure 3.7: Simple ADI with median subtraction for all data sets stacked.

### 3. RESULTS & DISCUSSION

---

For all analyses of simple ADI with mean or median subtraction, we checked the other apertures of the aperture ring for a  $S/N > 3$ . Of the 3448 apertures analyzed, 29 apertures had a  $S/N > 3$ . This points at the non-gaussian distribution of our data set, as we would expect an average occurrence of approximately 9 apertures with a  $S/N > 3$  for a Gaussian distribution.

#### 3.2.2 Flipped Derotation

Our simple ADI analyses were in a first step conducted with a wrongfully applied flip of the data sets. This analyses were used in the aftermath to test our statistical  $\sigma_x$  values, which should not be affected by rotating or mirroring the data.

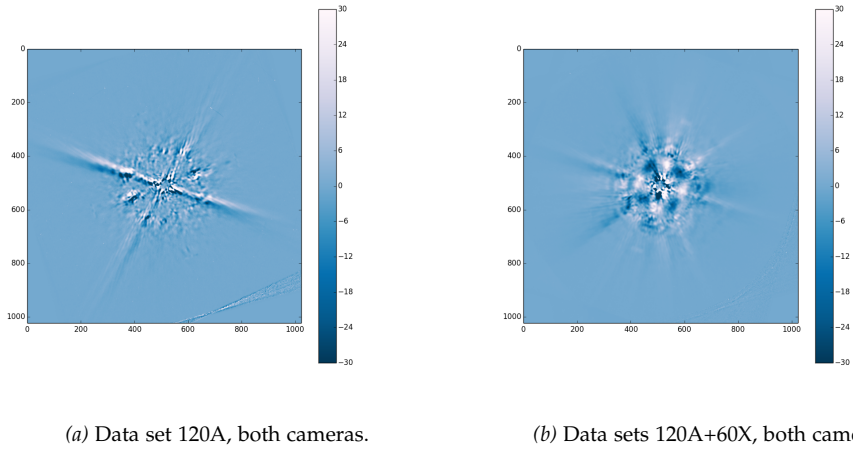


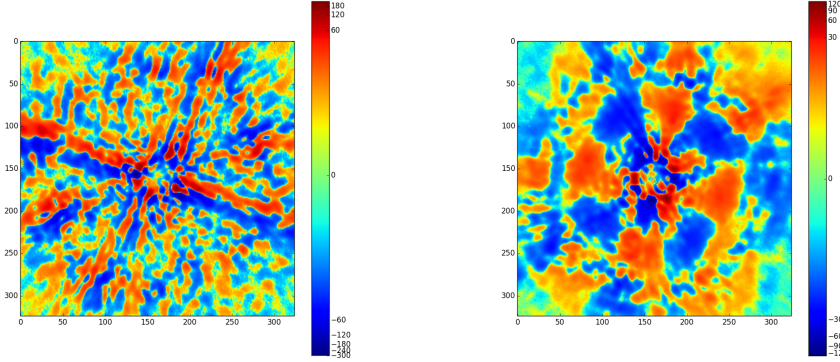
*Figure 3.8: FLIPPED Simple ADI applied to non-derotated data sets. Subtraction of mean and derotation in the aftermath.*

When comparing the figures 3.8 and 3.9 to 3.3 and 3.4 the geometric effect of the flipped simple ADI is clearly visible. When we look at the  $\sigma_x$ , the values are very similar though (see table 3.4). No systematic effects emerged.

Simple ADI		HR 8799 b	HR 8799 c	HR 8799 d	HR 8799 e
mean		1.89	12.67	26.52	145.71
mean, flipped		1.86	11.65	28.86	133.32
median		2.26	11.62	30.86	133.12
median, flipped		3.43	14.60	42.35	134.14

*Table 3.4: Standard deviation  $\sigma_x$  (counts) comparison for differently applied derotations and subtractions.*

Data sets 120A+60X, 40 apertures with  $r = 5$  px.



(a) Data set 120A, camera 1. (b) Data set 60X, camera 1.

Figure 3.9: FLIPPED, derotated and subtracted data in logarithmic scale.

### 3.2.3 Frame clipping

As the seeing and other factors influencing the quality of a single exposure change fast, we tried to apply a filter, to extract a selection of exposure frames with the best conditions. All frames were evaluated with an aperture ring of 40 apertures and a radius of  $r = 5$  px. The 60s exposure data was doubled, in order to get comparable standard deviation  $\sigma_x$ . Now we calculated the mean of all standard deviations:

$$\sigma_{mean} = \frac{\sum_{x=1}^i \sigma_x}{i} \quad (3.2)$$

$i$  was the number of analyzed exposure frames,  $i = 320$ . To apply a filter, we determined a standard deviation of the  $\sigma_x$ :

$$\sigma = \sqrt{\frac{1}{i-1} \sum_{x=1}^i (\sigma_x - \sigma_{mean})^2} \quad (3.3)$$

The exposure frames with a  $\sigma_x > \sigma_{mean} + \sigma$  were eliminated from the total data set. This procedure was applied for every exoplanet separately, leading to selected frames for HR 8799 b, HR 8799 c, HR 8799 d and HR 8799 e.

The remaining frames were again derotated, reduced by their mean and averaged as explained in section 3.2. The weights were adjusted to the remaining frames and their exposure time. We also applied search grids ( $20 \times 20$ px), to detect high flux areas in the vicinity of our astrometry locations. No areas with a  $S/N > 3$  were detected. The higher  $S/N$  of HR 8799 c are again due to the aberration feature of the mean subtraction in data set

### 3. RESULTS & DISCUSSION

---

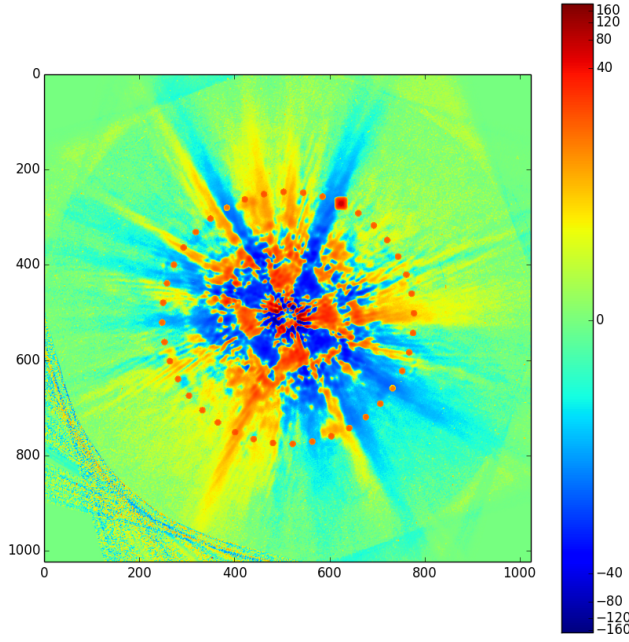


*Figure 3.10:* Exoplanet aperture, background apertures and search grid on selected frames, simple ADI reduced data for HR 8799 c. Data sets 120A + 60X, both cameras.

60X. Find the frame selected data logarithmically scaled in figure 3.10.

In a second analysis we applied the same selection criteria, without taking data set 120B into account. Therefore the number of analyzed exposure frames was reduced to  $i = 280$ . Again the frames with a  $\sigma_x > \sigma_{mean} + \sigma$  were eliminated (see equation 3.3). The remaining frames were derotated, reduced by the mean and averaged to a 120 s exposure frame. Again no  $S/N > 3$  areas were found within a grid of  $20 \times 20$  px around the astrometry positions (see table 3.5).

Data set	HR 8799 b	HR 8799 c	HR 8799 d	HR 8799 e
120A, 120B + 60X	-0.23	1.84	1.11	-0.47
120A + 60X	-0.03	2.17	1.09	0.08

*Table 3.5:*  $S/N$  for selected frames of the data sets; simple ADI with mean subtraction applied. 40 apertures with  $r = 5$  px.

When analyzing the clipped frames, one can see, that mainly the same frames on both cameras get clipped, predominantly over several consecutive frames. This points at atmospheric conditions, which lead to stronger speckle features for a short period of time. Most of these clusters were found close to the beginning and end of the data set observation times, providing an explanation for the visible derotation structure, when applying a simple ADI (see section 3.2).

Our quest to detect an exoplanet signal at a  $S/N > 3$  at our interpolated astrometric positions was conducted with several methods. The non-gaussian nature of our data was confirmed by this analysis.

Reduction of the aberration features by a simple ADI mean and median subtraction smoothened out the background, but diminished the exoplanet signal too. Some areas with high  $S/N$  ratios were still identified to be residuals of the PSF structure. No systematical difference of the background structure was detected between a mean or a median simple ADI subtraction. Some individual structures (like the speckle feature from the misplaced coronagraph in data set 120B) were suppressed better with the median subtraction. The systematic frame selection, based on the lowest standard deviation frames, did not provide a detection of an exoplanet signal either.

A flipped derotation of the data sets confirmed the rather statistical distribution of the background. No geometrical effects emerged. The frame selection showed that the speckles were mostly due to atmospheric disturbance, as the eliminated frames showed up mostly in both cameras simultaneously.

As we could not find an exoplanet signal, we did a comparison of the applied methods to our toy model in the next chapter. We conclude with an overview of the so far measured contrasts, expectations of the fitted models and our achieved contrast limits for all four exoplanets of the HR 8799 system and an outlook for future observations.



## Chapter 4

---

# Summary

---

So what did we learn from all these methods? Was there any improvement in the data analysis? To achieve a high  $S/N$ , or at a given  $S/N$  a low contrast detection limit, we have to analyze the variables contributing to our statistical analysis of the data. In the next sections we compare these values, which determine the achieved  $S/N$  and how they evolve, when applying the different methods.

The obtained  $\sigma_x$  and  $f_{mean}$  values, as well as the level of self-subtraction (median or mean frames applied), determine the contrast limit of the observation with our applied methods. A comparison of our contrast limits achieved to the observed contrasts of other HR 8799 system observations and models for hot giant planets follows up the method comparison section.

We conclude our thesis with an outlook of the necessary observation adaptations needed, to detect exoplanets in the long I band with direct imaging.

### 4.1 Contrast limit - Method comparison

To compare the values, which determine the achieved  $S/N$ , we have to analyze the contributing variables.

First of all we want to achieve a high exoplanet flux  $f_1$  with respect to the mean aperture flux  $f_{mean}$ . When stacking and averaging frames, we expect to achieve a stable  $f_1$  signal and at the same time (when considering a purely gaussian noise distribution) get a mean aperture flux  $f_{mean}$  converging to 0. This leads to a signal close to the flux of the exoplanet aperture.

The noise is given by the standard deviation  $\sigma_x$ . The more frames we stack and average, the lower the standard deviation should be. The prominent

## 4. SUMMARY

---

speckles of the single frames (if random enough) should cancel out. When applying a simple ADI reduction, the spyders (of the 2nd mirror mount) should vanish, as the whole structure of the fixed PSF is subtracted (details in 3.2).

### 4.1.1 Size and number of apertures

With the given PSF of the host star, we found a maximal  $S/N$  at an aperture size of  $r = 5\text{px}$ . All apertures at  $r \in [4, 7]$  provide a  $S/N$  within 10% of this maximum (see section 2.4).

When analyzing a single exposure, the amount of apertures reduces the standard deviation  $\sigma_x$  until a residual value is reached. If we add and average the single exposures, this has the same effect though. So for our analysis no significant reduction in the standard deviation was found when applying more apertures to derive it (see section 2.5.1). The same is true for the mean aperture flux  $f_{mean}$ . There was no significant trend towards 0, when applying more apertures. For the method comparison we therefore focused on the data analysis with 40 apertures of an aperture radius  $r = 5\text{ px}$ .

### 4.1.2 Toy model

In order to compare the retrieved data, we analyzed our toy models. The count results for a random PSF distribution (see section 2.4.1) normalized to a  $t = 120\text{s}$  exposure are listed in table 4.1 & 4.2.  $\sigma_x$  and  $f_{mean}$  are the determining factors of the  $S/N$  calculation.

Data set base	HR 8799 b	HR 8799 c	HR 8799 d	HR 8799 e
120A1	21.45	42.81	78.47	85.61
60X1	29.26	56.68	85.41	110.41

Table 4.1:  $\sigma_x$  (counts) of the toy model ( $t = 120\text{s}$ ) analysis based on different data sets; 40 apertures with  $r = 5\text{ px}$ .

Data set base	HR 8799 b	HR 8799 c	HR 8799 d	HR 8799 e
120A1	-0.10	-20.63	-27.02	-18.11
60X1	1.82	-23.47	-60.50	-28.98

Table 4.2:  $f_{mean}$  (counts) of the toy model ( $t = 120\text{s}$ ) analysis based on different data sets; 40 apertures with  $r = 5\text{ px}$ .

If we compare this to the 44'837'059 counts retrieved from the star analy-

## 4.1. Contrast limit - Method comparison

---

sis at  $r = 5$  px (see section 1.1), we get approximately 45 counts at a contrast of  $C = 10^{-6}$  for the expected exoplanet flux.

For the analysis of the different methods, we want to extract the contrast limit. We therefore solve equation 2.5 for the contrast  $C$ , with a simulated exoplanet flux  $f_{1,sim} = C \cdot f_{st}$  (see equation 2.7) replacing the exoplanet flux  $f_1$  in the equation.

$$C = \frac{\sigma_x(S/N) + f_{mean}}{f_{st}} \quad (4.1)$$

This does not take into account the self-subtraction of the planet flux and its correlated noise, when applying a simple ADI reduction.

For the method comparison we set a constant  $S/N = 3$  as this is the value we were probing for. The star flux is determined by our star observation with an aperture radius of  $r = 5$  px. This leads to the contrast limits of the toy models, factored for a single  $t = 120$  s exposure as shown in figure 4.1.

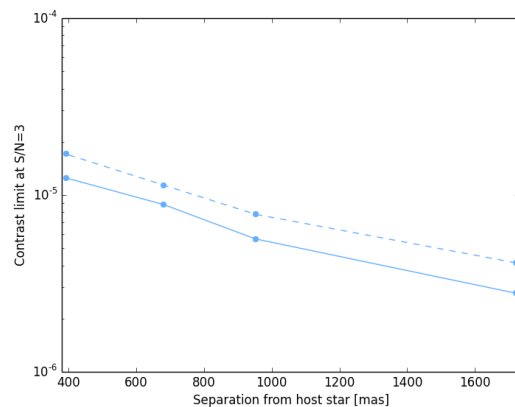


Figure 4.1: Our contrast limits for the toy model at a  $S/N = 3$ . The toy model is based on data set 120A, camera 1 (dashed line based on data set 60X, camera 1 factorized for a single  $t = 120$  s exposure).

### 4.1.3 Exposure time / Stacked frames

When we want to achieve a maximal exposure time, we have to combine the data sets. First we analyze the different data sets for their contrast limit. See figure 4.2 for the contrast limits of the averaged and derotated data sets.

The contrast limits for HR 8799 c, d and e are above the expected limit from the toy model for all data sets. The strong speckle features in this area are not gaussian distributed. For HR 8799 b further away from the host star

#### 4. SUMMARY

---

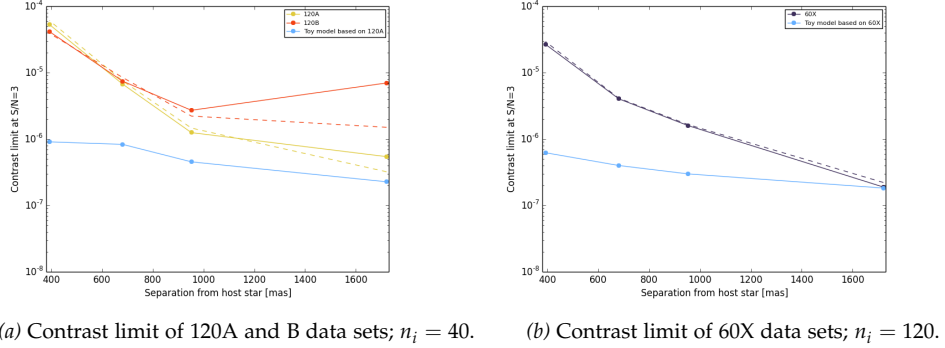


*Figure 4.2:* Our Contrast limits for the individual, averaged and derotated data sets at a  $S/N = 3$ . Solid lines: Data set camera 1; Dashed lines: Data set camera 2; Toy model factored by  $\frac{1}{\sqrt{n_i}}$ .

the asymmetric feature from the misplaced coronagraph in data set 120B is once again visible. The contrast of the other data sets is in the range of the toy model at this separation to the host star. Be aware, that the data set 60X has a much longer total exposure time ( $n_i = 120$ ) than the data sets 120A and 120B ( $n_i = 20$ ). The theoretical toy model contrast limits are therefore lower. The achieved contrast limit is only comparable low with respect to the toy model far away from the PSF structure for HR 8799 b. Closer to the host star, the strong aberration features almost cancel out the effects of the longer total exposure.

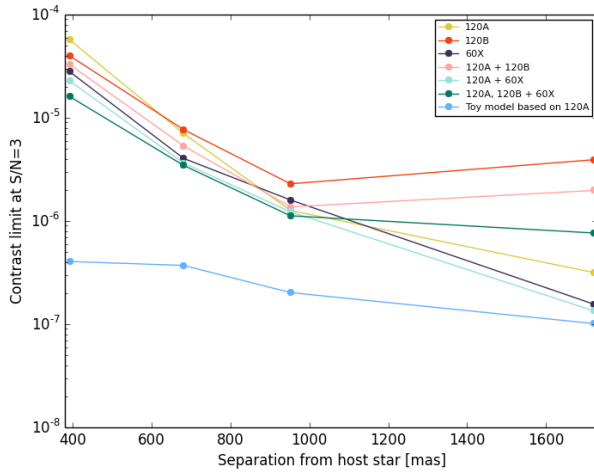


*Figure 4.3:* Our contrast limits for the individual and combined data sets (averaged and derotated; both cameras). Toy model factored by  $\frac{1}{\sqrt{n_i}}$ ;  $n_i = 200$ .

## 4.1. Contrast limit - Method comparison

If we combine the data sets, we get the contrast limits as shown in figure 4.3. The best contrast is achieved, when combining all data sets for the exoplanets HR 8799 c, d and e. The improvement to data set 120A is approximately at a factor 5 for HR 8799 e, at a factor 3 for HR 8799 d and below a factor 2 for HR 8799 c. For HR 8799 b the combination of data sets 120A and 60X gives the best contrast limit. It is improved by a factor 3 compared to the values of data set 120A.

The lowering of the contrast limit is in the range of the expected lowering of a 5 times longer total exposure time, which leads to a lowering of the contrast of  $\sqrt{5} \simeq 2.24$ .

### 4.1.4 Simple ADI / Frame selection

The reduction of our frames with the mean/median of the data set and derotation in the aftermath should further improve our contrast limit. The contrast limits achieved by this method are shown in figure 4.4a

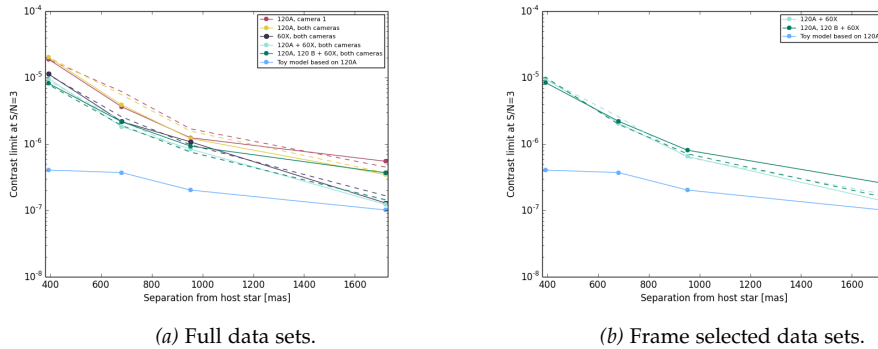


Figure 4.4: Our contrast limits for simple ADI reduced data sets.

Toy model factored by  $\frac{1}{\sqrt{n_i}}$ ;  $n_i = 200$

Solid lines: mean subtraction; Dashed lines: median subtraction.

For the set, where all data was combined and a simple ADI mean subtraction was applied, we achieve a contrast limit at a factor 2 lower than with the stacked derotated averaged frames. With this method the contrast limit for HR 8799 c is approximately at a  $C = 2 \cdot 10^{-6}$ . No systematical effect is found between the median or mean subtraction method, except for the combination with data set 120B applied at separation of HR 8799 b. The prominent speckle features there are suppressed better with the median subtraction.

When applying the frame selection to our data, the achieved contrast limits

## 4. SUMMARY

---

were slightly higher with respect to the simple ADI method for the combined data sets (see figure 4.4b). They are within a margin of a few % though. Only for the combination of all data sets in the range of HR 8799 b the frame selection improves the contrast limit through elimination of the strongest aberration features in this data set. The frame selection does in general not lead to a significant change in contrast limit. The abundance of the total set and its improvement of the data due to the subtraction of the mean or median seems to outweigh the reduction of the selected frames.

### 4.1.5 Noise distribution

As we used a statistic approach to our data, we considered the background to be normally distributed. In our applied methods we found several hints, that this is not entirely the case. If we look at the Q-Q-Plots of our data for HR 8799 c (see figure 4.5), we can see, that with the applied methods, the background approaches a gaussian distribution. The assumption, that it is completely gaussian is not reached though and this has to be taken into account, when considering the contrast limits achieved.

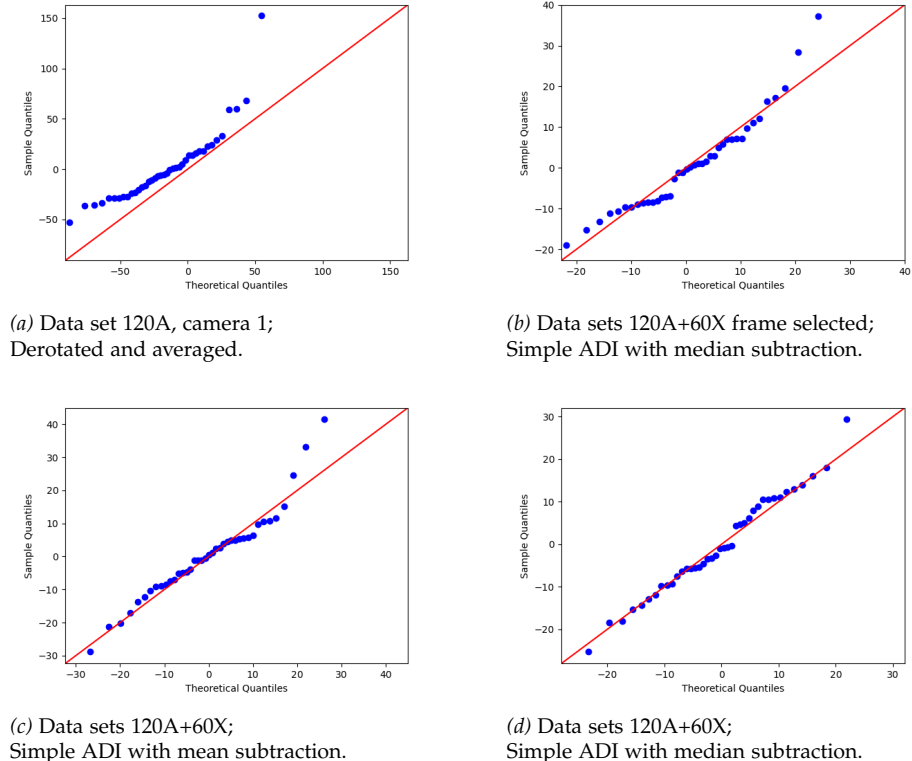


*Figure 4.5:* Q-Q-Plots for the aperture flux measurements of the background apertures for HR 8799 c. 40 apertures,  $r = 5 \text{ px}$ .

## 4.2 Contrast limit - Comparison to published measured and modeled data

The HR 8799 system has been observed by several instruments and in different wavebands. In order to compare our contrast limits to the data obtained in published detection results, we had to first set a framework for this comparison. A wide variety of absolute flux, measured flux, theoretical flux, as well as contrast measurements was published in the reference data. To get an overview of the measured intensity of the planets, we had to calculate the contrast of the measured planet flux to the star flux of HR 8799 in the corresponding waveband.

For the host star HR 8799 we set the synthetic ATLAS9 spectrum as a reference, as done by [Zurlo et al., 2016]. The ATLAS9 Model grid by [Castelli and Kurucz, 2004] was scaled to fit the Tycho2 BV, 2MASS JHKS, and WISEW1W2 photometry ([Høg et al., 2000], [Cutri et al., 2012]) with  $T_{eff} = 7500\text{ K}$ ,  $\log g = 4.5$ ,  $M/H = 0$ ,  $v_{turb} = 0 \frac{\text{km}}{\text{s}}$ . We converted the data into absolute flux values:

$$F_\lambda = f_\lambda \frac{d^2}{d_V^2} \quad (4.2)$$

and got the reference host star values as stated in table 4.3.  $f_\lambda$  is the apparent flux of HR 8799 and  $d_V = 10\text{ pc}$  is the calibrated distance to Vega. Our distance to HR 8799 is  $d = 41.2925\text{ pc}$  [Universite de Strasbourg/CNRS, 2021]. The contrast values were obtained, by dividing the measured absolute flux

Wavelength [ $\lambda$ ]	Absolute Flux [ $10^{-10} \frac{\text{W}}{\text{m}^2 \mu\text{m}}$ ]
0.9	9.4
1.0	6.8
1.1	6.0
1.2	4.6
1.3	3.4
1.4	2.6
1.5	2.2
1.6	1.9
1.7	1.7
1.8	1.4
1.9	1.0
2.0	0.7

Table 4.3: Applied synthetic absolute flux  $F_\lambda$  of the host star HR 8799 based on the ATLAS9 model.

#### 4. SUMMARY

---

values of the planets (or the apparent flux values converted into absolute flux values) with the host star reference flux values of table 4.3.

$$C = \frac{F_{\lambda,planet}}{F_{\lambda,star}} \quad (4.3)$$

The measured data which were used for our comparison are the following:

- IRDIS - measurement by [Zurlo et al., 2016]
- IFS - measurement by [Zurlo et al., 2016] (for HR 8799 d and e)
- Marois - [Marois et al., 2008] (for HR 8799 b, c and e)
- Currie - [Currie et al., 2011] (for HR 8799 b, c and d)
- Skemer - [Skemer et al., 2012]
- GPI - [Greenbaum et al., 2018] (for HR 8799 c, d and e)
- GRAVITY - [Lacour et al., 2019] (for HR 8799 e only)

As the exoplanets have not yet been imaged in our waveband, we used the model data below to get an estimate with respect to our contrast limit:

- CoolITLusty - described and applied in [Hubeny and Lanz, 1995], used by [Lacy and Burrows, 2020]  
Generally assumes a condensate-free, solar metallicity atmosphere.  
The used inputs to the code are:

- The stellar spectral type of HR 8799 (incoming irradiation): A5V
- The semimajor axis:  $HR 8799 d = 27 \text{ au}$ ,  $HR 8799 e = 16.4 \text{ au}$
- The planet radius:  $HR 8799 d = 1.35 R_J$ ,  $HR 8799 e = 1.17 R_J$
- The planet surface gravity:  $\log g = 4$
- The planet effective temperature [ $T_{eff}$ ]:  $HR 8799 d = 1000 \text{ K}$ ,  $HR 8799 e = 1150 \text{ K}$
- Exo-REM - described and applied in [Charnay et al., 2017], used by [Baudino et al., 2017] and [Lacour et al., 2019].  
The used inputs to the code are:
  - The planet surface gravity [ $\log g$ ]:  $HR 8799 b = 4.8 \pm 0.4$ ,  $HR 8799 c = 4.95 \pm 0.45$ ,  $HR 8799 d = 5.0 \pm 0.4$ ,  $HR 8799 e = 4.7 \pm 0.7$
  - The planet effective temperature [ $T_{eff}$ ]:  $HR 8799 b = 975 \text{ K} \pm 225$ ,  $HR 8799 c = 1125 \text{ K} \pm 225$ ,  $HR 8799 d = 1125 \text{ K} \pm 75$ ,  $HR 8799 e = 1200 \text{ K} \pm 150$

## 4.2. Contrast limit - Comparison to published measured and modeled data

- petitRADTRANS - described and applied in [Molliere et al., 2020] Retrieval model with 18 free parameters (Temperature profile; Photon pressure; Opacity; Element composition; Gravitational force, etc.) for the atmospheric properties of HR 8799 e. Based on photometric data from the SPHERE ([Zurlo et al., 2016], GPI ([Greenbaum et al., 2018]) and GRAVITY observations ([Lacour et al., 2019]).

The models are based on the (at time of publication) available photometric measurements. The currently accepted assumptions of **surface** temperatures are  $T = 600\text{ K}$  for HR 8799 b and  $T = 800\text{ K}$  for HR 8799 c, d and e. The expected masses for the exoplanets are  $M = 7M_J$  for HR 8799 b,  $M = 8.3M_J$  for HR 8799 c and d and  $M = 9.6M_J$  for HR 8799 e [Henry, 2021]. The models take clouds with different substance absorption into account. Find more details in the respective reference papers.

In the following sections the values for each exoplanet of the HR 8799 system are discussed. The data are bound to rounding errors and should be interpreted as estimates within orders of magnitude.

### 4.2.1 HR 8799 b

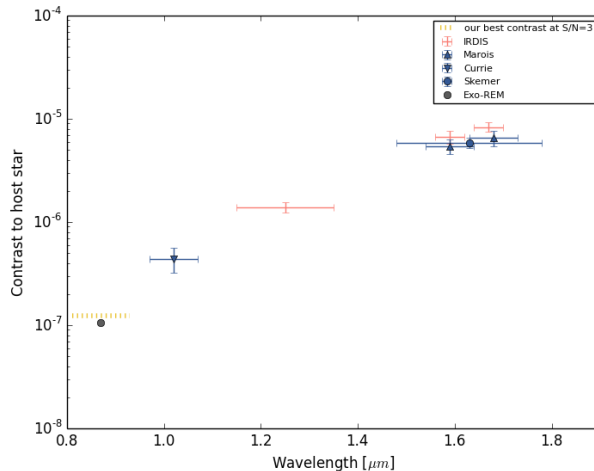


Figure 4.6: Measured and modeled contrasts and contrast limits - HR 8799 b.

For the outermost planet we achieved the lowest contrast limit. It is the planet, which has the least impact by speckles and other aberrations and therefore our contrast limit was in the same range as the theoretical expected contrast limit (see section 4.1).

Our limit is well below the contrasts measured so far for this planet, as

## 4. SUMMARY

---

you can see in figure 4.6. When we have a look at the expected modeled data, we can see, that our contrast limit is just above the expected contrast of this exoplanet. In a close up noise map of the best contrast data (data set 60X, simple ADI, median subtraction), no clear structure is visible (see figure 4.7; The astrometry position of HR 8799 b is centered).

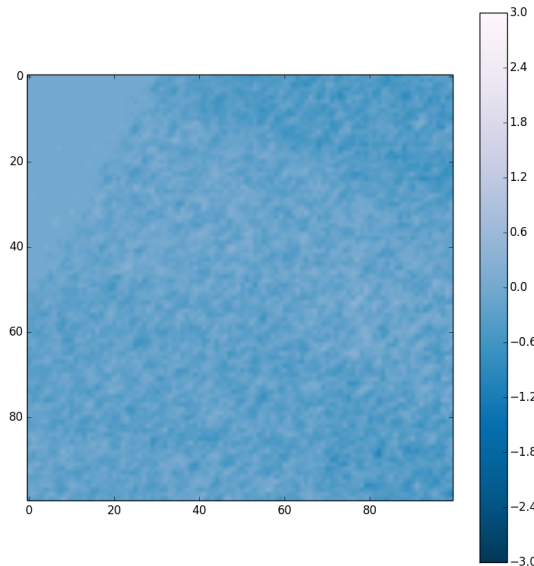


Figure 4.7: Noise map of HR 8799 b - Data set 60X, simple ADI, median subtraction.

### 4.2.2 HR 8799 c

Our most promising candidate, when starting our analysis, seemed HR 8799 c. When comparing our contrast limit to the measured data so far (see figure 4.8) this hypothesis still holds. The upper limit of [Currie et al., 2011] shows, that the contrast at shorter wavelengths must fall off rather rapidly though.

When we have a look at the expected contrast of the modeled data, we see, that we reach a contrast limit just below the expected contrast of this exoplanet. As shown in section 3.2 and following, we were not able to detect a stable  $S/N > 3$  with this contrast limit. Further the close up noise maps show no visible structures after the applied methods (see figure 3.6).

As we considered a  $S/N = 3$  to achieve this limit and as the calculations are bound to several transforming and rounding errors, the achieved contrast

## 4.2. Contrast limit - Comparison to published measured and modeled data

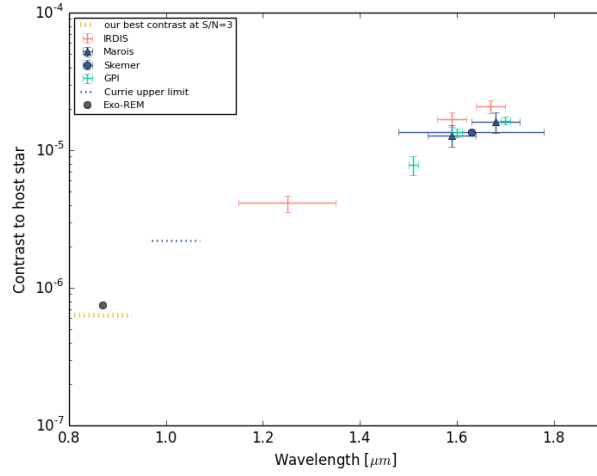


Figure 4.8: Measured and modeled contrasts and contrast limits - HR 8799 c.

limit is rather a lowest possible estimate. Also the subtraction of part of the exoplanet signal was not taken into account, when applying the simple ADI subtractions. The non-detection of a signal is therefore not surprising and within the error of our estimations and calculations.

### 4.2.3 HR 8799 d

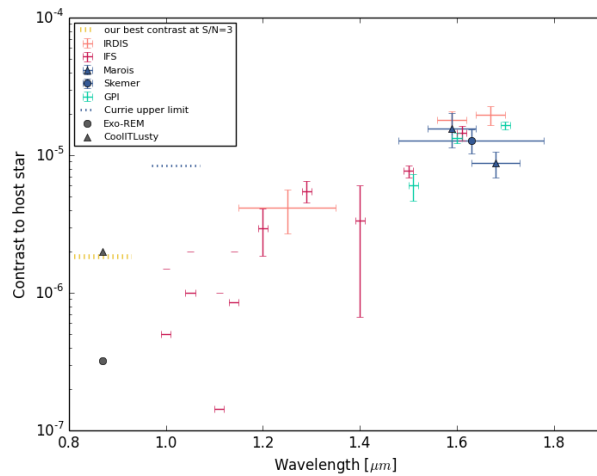


Figure 4.9: Measured and modeled contrasts and contrast limits - HR 8799 d.

The contrast limit for a  $S/N = 3$  of our data is approximately at the same level of the measured data in the near-IR band (see figure 4.9) for HR 8799 d.

## 4. SUMMARY

---

The IFS data close to our waveband are within our contrast limit. The wide error-bars of the IFS data at this low wavelengths as well as the upper limit of [Currie et al., 2011] hint at a drop in contrast for these shorter wavelengths though.

The models predict signals, which are almost a magnitude of contrast apart. Even the highest predicted contrast taken into consideration is just above our contrast limit, therefore we cannot rule this model out with our calculations.

### 4.2.4 HR 8799 e

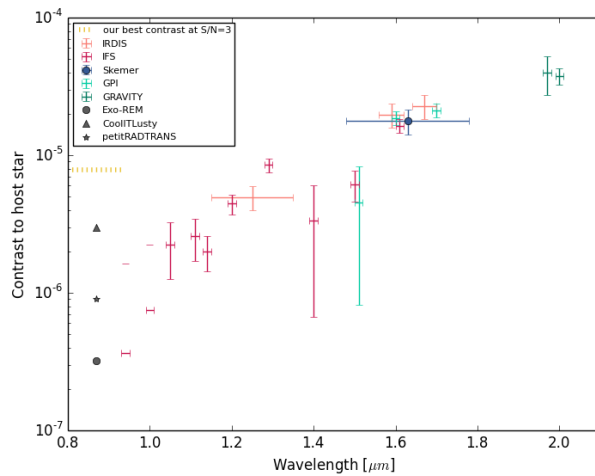


Figure 4.10: Measured and modeled contrasts and contrast limits - HR 8799 e.

Our contrast limit for HR 8799 e is rather high. The speckle rings and aberrations close to the host star make it not very likely to find a signal in our data at this separation. Compared to the measured data in figure 4.10 we need a much lower contrast limit in this waveband to detect an exoplanet signal.

Also the modeled contrasts are all well below our contrast limit and therefore not much conclusions can be made for this planet.

## 4.3 Outlook

When looking for a directly imaged exoplanet signal in the visible light, the contrast limit is probably the most crucial factor. To achieve a low contrast limit, simple ADI subtraction is a method which can lower the contrast limit

### 4.3. Outlook

by a factor 2 with respect to derotated, averaged and stacked observation frames. Longer exposure times and a high number of individual frames can lower the contrast limit more significantly. In our data this lowered the contrast limit within a factor of 2-5 with respect to a single data set, depending on the separation of the object to the host star. This factor is in the range of the expected theoretical factor for the longer exposure time. We have to take into account, that the combination of both cameras, who observed simultaneously, is not lowering the contrast limit. To achieve the desired improvement in contrast, one has to observe at different times.

Therefore, in order to reach the modeled contrast limits for HR 8799 b and HR 8799 c, a four times longer total observation time could result in a detection. For HR 8799 d and especially for HR 8799 e a detection in the visible range seems rather unlikely, given the pronounced gap between the modeled contrast limit and the achieved contrast limit in this observation. To reduce the read out noise, contributing strongly especially for the exoplanets furthest away from the host star, longer individual frame observation times would be favorable.

Our applied methods of data reduction were rather simple and should give an estimate on the necessary observation time and the possible contrast limit with the ZIMPOL imager in the long I band. More sophisticated data extraction can further improve the achieved contrast limit. Combined with longer observation time a detection of young self-emitting exoplanets with this instrument should be feasible.



---

## Bibliography

---

- [Apai et al., 2016] Apai, D., Kasper, M., Skemer, A., et al. (2016). High-cadence, high-contrast imaging for exoplanet mapping: Observations of the hr 8799 planets with vlt/sphere satellite-spot-corrected relative photometry. *The Astrophysical Journal*, 820:40–52.
- [Baudino et al., 2017] Baudino, J.-L., Bonnefoy, M., Vigan, A., et al. (2017). Characterising exoplanet atmospheres with sphere: The hr 8799 system with exo-rem and nemesis. *SF2A*.
- [Castelli and Kurucz, 2004] Castelli, F. and Kurucz, R. L. (2004). New grids of atlas9 model atmospheres. *IAU Symposium*.
- [Charnay et al., 2017] Charnay, B., Bezard, B., Baudino, J.-L., et al. (2017). A self-consistent cloud model for brown dwarfs and young giant exoplanets: comparison with photometric and spectroscopic observations. *The Astrophysical Journal*, 854.
- [Currie et al., 2011] Currie, T., Burrows, A., Itoh, Y., and et al. (2011). A combined subaru/vlt/mmt 1-5  $\mu$ m study of planets orbiting hr 8799: Implications for atmospheric properties, masses, and formation. *The Astrophysical Journal*, 729:128.
- [Cutri et al., 2012] Cutri, R. M. et al. (2012). Vizier online data catalog: Wise all-sky data release. <https://ui.adsabs.harvard.edu/abs/2012yCat.2311....0C/abstract>.
- [de Rosa et al., 2020] de Rosa, R. J., Nguyen, M. M., Chilcote, J., et al. (2020). Revised astrometric calibration of the gemini planet imager. *Journal of Astronomical Telescopes, Instruments, and Systems*, 6.

## BIBLIOGRAPHY

---

- [Greenbaum et al., 2018] Greenbaum, A. Z., Pueyo, L., Ruffio, J.-B., et al. (2018). Gpi spectra of hr 8799 c, d, and e from 1.5 to 2.4  $\mu\text{m}$  with klip forward modeling. *The Astronomical Journal*, 155:226–246.
- [Henry, 2021] Henry, F. (last checked August 18th, 2021). Exoplanet.eu by the europlanet 2020 research infrastructure project. [http://exoplanet.eu/catalog/hr\\_8799\\_b/](http://exoplanet.eu/catalog/hr_8799_b/).
- [Høg et al., 2000] Høg, E., Fabricius, C., Makarov, V. V., et al. (2000). The tycho-2 catalogue of the 2.5 million brightest stars. *Astron. Astrophys.*, 355:27–30.
- [Howell, 1989] Howell, S. (1989). Two-dimensional aperture photometry: Signal-to-noise ratio of point-source observations and optimal data-extraction techniques. *Publications of the Astronomical Society of the Pacific*, 101:616–622.
- [Hubeny and Lanz, 1995] Hubeny, I. and Lanz, T. (1995). Non-lte line-blanketed model atmospheres of hot stars. i. hybrid complete linearization/accelerated lambda iteration method. *The Astrophysical Journal*, 439:875–904.
- [Lacour et al., 2019] Lacour, S., Nowak, M., Wang, J., et al. (2019). First direct detection of an exoplanet by optical interferometry astrometry and k-band spectroscopy of hr 8799 e. *Astronomy + Astrophysics*, 623:11.
- [Lacy and Burrows, 2020] Lacy, B. and Burrows, A. (2020). Prospects for directly imaging young giant planets at optical wavelengths. *The Astrophysical Journal*, 892:151.
- [Marois et al., 2008] Marois, C., Macintosh, B., Barman, T., et al. (2008). Direct imaging of multiple planets orbiting the star hr 8799. *Science*, 322:1348–1352.
- [Marois et al., 2010] Marois, C., Zuckerman, B., Konopacky, Q. M., et al. (2010). Images of a fourth planet orbiting hr 8799. *Nature*, 468:1080–1083.
- [Molliere et al., 2020] Molliere, P., Stolker, T., Lacour, S., et al. (2020). Retrieving scattering clouds and disequilibrium chemistry in the atmosphere of hr 8799e. *Astronomy + Astrophysics*, 640.
- [Schmid et al., 2018] Schmid, H. M., Bazzon, A., Roelfsema, R., et al. (2018). Sphere/zimpol high resolution polarimetric imager - i. system overview, psf parameters, coronagraphy, and polarimetry. *Astronomy + Astrophysics*, 619:A9.

## Bibliography

---

- [Skemer et al., 2012] Skemer, A. J., Hinz, P. M., Esposito, S., et al. (2012). First light lbt ao images of hr 8799 bcde at 1.6 and 3.3  $\mu$ m: New discrepancies between young planets and old brown dwarfs. *The Astrophysical Journal*, 753:14.
- [Thalmann et al., 2008] Thalmann, C., Schmid, H. M., Boccaletti, A., et al. (2008). Sphere-zimpol view project matisse view project sphere zimpol: Overview and performance simulation. *SPIE*.
- [Universite de Strasbourg/CNRS, 2021] Universite de Strasbourg/CNRS (last checked August 8th, 2021). SIMBAD astronomical database - cds (strasbourg). <http://simbad.u-strasbg.fr/simbad/sim-id?Ident=HR%208799&NbIdent=1&Radius=2&Radius.unit=arcmin&submit=submit%20id>.
- [Wahhaj et al., 2021] Wahhaj, Z., Milli, J., Romero, C., et al. (2021). A search for a fifth planet around hr 8799 using the star-hopping rdi technique at vlt/sphere. *Astronomy + Astrophysics*, 648:26.
- [Wang et al., 2018] Wang, J. J., Graham, J. R., Dawson, R., et al. (2018). Dynamical constraints on the hr 8799 planets with gpi. *The Astronomical Journal*, 156:192–209.
- [Zurlo et al., 2016] Zurlo, A., Vigan, A., Galicher, R., et al. (2016). Astrophysics first light of the vlt planet finder sphere iii. new spectrophotometry and astrometry of the hr 8799 exoplanetary system. *Astronomy + Astrophysics*, 587:57.

## Declaration of originality

The signed declaration of originality is a component of every semester paper, Bachelor's thesis, Master's thesis and any other degree paper undertaken during the course of studies, including the respective electronic versions.

Lecturers may also require a declaration of originality for other written papers compiled for their courses.

---

I hereby confirm that I am the sole author of the written work here enclosed and that I have compiled it in my own words. Parts excepted are corrections of form and content by the supervisor.

**Title of work** (in block letters):

HR 8799 imaged in the long I band

**Authored by** (in block letters):

*For papers written by groups the names of all authors are required.*

**Name(s):**

Gisin

**First name(s):**

Dominique

With my signature I confirm that

- I have committed none of the forms of plagiarism described in the '[Citation etiquette](#)' information sheet.
- I have documented all methods, data and processes truthfully.
- I have not manipulated any data.
- I have mentioned all persons who were significant facilitators of the work.

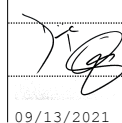
I am aware that the work may be screened electronically for plagiarism.

**Place, date**

Zürich, 13. September 2021

**Signature(s)**

Verified by PDFFiller



09/13/2021

*For papers written by groups the names of all authors are required. Their signatures collectively guarantee the entire content of the written paper.*